

# High-resolution calculation of the solar global convection with the reduced speed of sound technique: II. Near surface shear layer with the rotation

H. Hotta<sup>1,2</sup>, M. Rempel<sup>1</sup>, and T. Yokoyama<sup>2</sup>

<sup>1</sup>High Altitude Observatory, National Center for Atmospheric Research, Boulder, CO, USA

<sup>2</sup>Department of Earth and Planetary Science, University of Tokyo, 7-3-1 Hongo,  
Bunkyo-ku, Tokyo 113-0033, Japan

`hotta@ucar.edu`

Received \_\_\_\_\_; accepted \_\_\_\_\_

## ABSTRACT

We present a high-resolution, highly stratified numerical simulation of rotating thermal convection in a spherical shell. Our aim is to study in detail the processes that can maintain a near surface shear layer (NSSL) as inferred from helioseismology. Using the reduced speed of sound technique we can extend our global convection simulation to  $0.99 R_{\odot}$  and include near the top of our domain small-scale convection with short time scales that is only weakly influenced by rotation. We find the formation of a NSSL preferentially in high latitudes in the depth range  $r = 0.95 - 0.975 R_{\odot}$ . The maintenance mechanisms are summarized as follows. Convection under weak influence of rotation leads to Reynolds stresses that transport angular momentum radially inward in all latitudes. This leads to the formation of a strong poleward directed meridional flow and a NSSL, which is balanced in the meridional plane by forces resulting from the  $\langle v'_r v'_\theta \rangle$  correlation of turbulent velocities. The origin of the required correlations depends to some degree on latitude. In high latitudes a positive correlation  $\langle v'_r v'_\theta \rangle$  is induced in the NSSL by the poleward meridional flow whose amplitude increases with the radius, while a negative correlation is generated by the Coriolis force in bulk of the convection zone. In low latitudes a positive correlation  $\langle v'_r v'_\theta \rangle$  results from rotationally aligned convection cells (“banana cells”). The force caused by these Reynolds stresses is in balance with the Coriolis force in the NSSL.

*Subject headings:* Sun: interior — Sun: dynamo — Stars: interiors

## 1. Introduction

The Sun is rotating differentially. The detailed distribution of the angular velocity is revealed by helioseismology (Thompson et al. 2003; Howe 2009; Howe et al. 2011, see Fig. 1). The three important findings by helioseismology are the tachocline, the conical profile in the middle of the convection zone, and the near surface shear layer (NSSL). The physical mechanism underlying these features is discussed in the next section. The three features show a significant deviation from the expected Taylor-Proudman state where the angular velocity does not change along the rotational axis. The strongest deviations from the Taylor-Proudman state are found in the two boundary layers, the tachocline and the NSSL. As shown in Fig. 1, the thickness of the NSSL is about  $0.04R_{\odot}$ , where  $R_{\odot}$  is the solar radius. The difference of the angular velocity ( $\Omega/(2\pi)$ ) in the region is 10-20 nHz. The variation in latitude is not significant in the NSSL (Fig. 1b). The existence of the NSSL was already inferred before the advent of helioseismology. Foukal & Jokipii (1975) pointed out that magnetic structures rotate 5 % faster than surrounding gas. Then Howard et al. (1984) compared the rotation rate estimated from the Doppler velocity measurement and the tracking of the sunspots. It was found that the rotation rate of the sunspots is consistently faster than the Doppler velocity. This was interpreted as an indication that the sunspots are anchored in a faster-rotating deeper layer.

### 1.1. Maintenance of the differential rotation

According to Miesch & Hindman (2011), the mean flows in the convection zone are described by the two equations, which are the gyroscopic pumping and the meridional force balance. The discussion below is in the spherical geometry  $(r, \theta, \phi)$ . The gyroscopic pumping is derived from the zonal component of the equation of motion with the anelastic

approximation ( $\nabla \cdot (\rho_0 \mathbf{v}) = 0$ ) as:

$$\rho_0 \frac{\partial \langle \mathcal{L} \rangle}{\partial t} = -\rho_0 \langle \mathbf{v}_m \rangle \cdot \nabla \langle \mathcal{L} \rangle + \mathcal{F}_R, \quad (1)$$

where  $\rho_0$ ,  $\mathbf{v}_m$ , and  $\mathcal{L} = r \sin \theta u_\phi$  specify the background density, the meridional flow, and the specific angular momentum.  $\mathbf{v}$  and  $\mathbf{u}$  specify the fluid velocities at the rotating system and the inertial reference system, respectively, i.e.,  $\mathbf{u} = \mathbf{v} + r \sin \theta \Omega_0 \mathbf{e}_\phi$ , where  $\Omega_0$  and  $\mathbf{e}_\phi$  are the rotation rate of the system and the zonal unit vector. The bracket  $\langle \rangle$  indicates the average in time and zonal direction. In this discussion, the magnetic field and the viscosity are neglected. Then the term  $\mathcal{F}_R$  is expressed as:

$$\mathcal{F}_R = -\nabla \cdot (\rho_0 r \sin \theta \langle \mathbf{v}'_m v'_\phi \rangle), \quad (2)$$

where prime indicates the deviation from the axisymmetric temporally averaged value, i.e., a value is divided as  $Q = \langle Q \rangle + Q'$ .  $\mathcal{F}_R$  expresses the angular momentum transport by the Reynolds stress, i.e., the non-linear coupling of the convective flow components. The gyroscopic pumping equation indicates that when the correlation of the convection flow is determined, the mean meridional flow is determined accordingly in the steady state ( $\partial/\partial t = 0$ ).

The detailed derivation of the meridional force balance is found in Appendix C.

$$\frac{\partial \langle \omega_\phi \rangle}{\partial t} = [\langle \nabla \times (\mathbf{v} \times \omega) \rangle]_\phi + 2r \sin \theta \Omega_0 \frac{\partial \langle \Omega_1 \rangle}{\partial z} + \frac{g}{\rho_0 r} \left( \frac{\partial \rho}{\partial s} \right)_p \frac{\partial \langle s_1 \rangle}{\partial \theta}, \quad (3)$$

where  $\omega = \nabla \times \mathbf{v}$ ,  $\Omega_1 = v_\phi/(r \sin \theta)$ ,  $g$ , and  $s$  are the vorticity, the angular velocity, the gravitational acceleration, and the entropy, respectively. The subscript 0 and 1 show the background and perturbed values, respectively.  $z$  means the direction of the rotational axis. The first term expresses the transport and the stretching which includes both contributions of mean flow and turbulent flow (we call it transport term). The second term shows the Coriolis force on the meridional plane and the third is the baroclinic term.

We discuss the NSSL with these two equations. Foukal & Jokipii (1975) suggest that when the convection is not influenced much by the rotation, the radial velocity in the thermal convection transports the angular momentum radially inward (Fig. 2). When the influence from the rotation is weak and the radial motion conserves the angular momentum, the correlation  $\langle v'_r v'_\phi \rangle$  is negative and transport angular momentum radially inward. Foukal & Jokipii (1975) argued that this is the process for the generation and maintenance of the NSSL (see also Gilman & Foukal (1979)). There have been several attempts to reproduce the NSSL based on this assumption (De Rosa et al. 2002; Rempel 2005; Brandenburg 2007; Guerrero et al. 2013).

Miesch & Hindman (2011), however, showed that the radially inward angular momentum transport by the Reynolds stress is only a necessary condition and that the force balance in the meridional plane must be considered in addition. When the transport term and the baroclinic term in eq. (3) are neglected, the meridional force balance equation becomes

$$\frac{\partial \langle \omega_\phi \rangle}{\partial t} = 2r \sin \theta \Omega_0 \frac{\partial \langle \Omega_1 \rangle}{\partial z}. \quad (4)$$

This means that when the radially inward angular momentum transport generates the NSSL especially from mid to high latitudes, i.e., negative  $\partial \langle \Omega_1 \rangle / \partial z$ , it creates an anti-clockwise meridional flow. This meridional flow continues to be accelerated and transport the angular momentum, until  $\partial \langle \Omega_1 \rangle / \partial z$  becomes zero. Thus, in order to obtain a meridional force balance that breaks the Taylor-Proudman constraint, other terms are necessary to compensate the Coriolis force. For instance, it is thought that the baroclinic term balances the Coriolis force within the bulk of the convection zone, which may lead to the conical profile of the solar differential rotation and the structure of the tachocline observed there (Rempel 2005; Miesch et al. 2006; Brun et al. 2011; Hotta & Yokoyama 2011). Balbus (2009) obtained the solar-like differential rotation with this idea and the assumption that

isentropic and isorotational surfaces coincide. Regarding the NSSL, it is unlikely that the baroclinic term is larger than that in the middle of the convection zone. Even if so, the expected temperature would be 10 K at the surface, which is not seen in observations (e.g. Rast et al. 2008). The transport term could play essential role in maintaining the NSSL. In the near surface layer, the convection speed increases and the spatial scale decreases. Indeed, it is expected that the ratio of the rotational period to the convective dynamical time scale (i.e., the Rossby number  $Ro$ ) should grow larger in the NSSL relative to the low Rossby number ( $Ro < 1$ ) convection of the deep interior due to the decreasingly small overturning time of convection near the surface. Thus, the reproduction of the NSSL in the numerical calculation requires a wide range of spatial and temporal scales, which must include giant cells down to scales smaller than supergranulation. Our previous study of non-rotating global convection was successful in capturing convective scales smaller than supergranulation in the near surface layer using the reduced speed of sound technique (Hotta et al. 2014, : hereafter Paper I). In this study, we include the rotation to reproduce the NSSL in the global convection calculation. The main focus of this paper is to clarify the generation and maintenance mechanism of the NSSL in the view of the dynamical balance on the meridional plane as well as the angular momentum transport.

## 2. Model

We solve three-dimensional hydrodynamic equations in the spherical geometry  $(r, \theta, \phi)$ :

$$\frac{\partial}{\partial t}(\xi^2 \rho_1) = -\nabla \cdot (\rho \mathbf{v}), \quad (5)$$

$$\rho \frac{\partial \mathbf{v}}{\partial t} = -\rho(\mathbf{v} \cdot \nabla) \mathbf{v} - \nabla p_1 - \rho_1 g \mathbf{e}_r + 2\rho \mathbf{v} \times \boldsymbol{\Omega}_0, \quad (6)$$

$$\rho T \frac{\partial s_1}{\partial t} = -\rho T(\mathbf{v} \cdot \nabla) s_1 + \frac{1}{r^2} \frac{d}{dr} \left( r^2 \kappa_r \rho_0 c_p \frac{dT_0}{dr} \right) + \Gamma, \quad (7)$$

$$p_1 = \left( \frac{\partial p}{\partial \rho} \right)_s \rho_1 + \left( \frac{\partial p}{\partial s} \right)_\rho s_1, \quad (8)$$

where  $\rho = \rho_0 + \xi^2 \rho_1$ . The numerical model is similar to Paper I. We adopt the new expression of reduced speed of sound technique (Hotta et al. 2012b, see also Appendix A) and the equation of state including the partial ionization effect for the Sun.  $\Gamma$  is the cooling term, which is effective only near the surface. We include the effect of rotation with a rate of  $\Omega_0/(2\pi) = 413$  nHz, which is the solar rotation rate. We adopt the same artificial viscosity as Rempel (2014). The details are shown in Appendix B. The same distribution of  $\xi$  is used as Paper I, which is defined as:

$$\xi(r) = \xi_0 \frac{c_s}{c_s(r_{\min})}, \quad (9)$$

where the adiabatic speed of sound is defined  $c_s = \sqrt{(\partial p / \partial \rho)_s}$  and  $\xi_0 = 200$  is adopted. Using this, the reduced speed of sound is  $1.13 \text{ km s}^{-1}$  at all depth. The distribution of  $\xi$  is shown in Fig. 3. The initial stratification is adiabatic  $ds_0/dr = 0$ , and a small perturbation is added to the entropy in order to start convection. The radiative diffusivity is 18 times smaller than that calculated in the Model S (Christensen-Dalsgaard et al. 1996); thus the imposed luminosity is also 18 times smaller than the solar luminosity. When we use the low viscosity in combination with the solar rotation rate and luminosity, the polar region is accelerated rather than the equator (Fan et al. 2013). There have been some systematic investigation on the relation between the Rossby number and rotation profile (Käpylä et al. 2011; Matt et al. 2011; Gastine et al. 2014). The formation of the NSSL, however, requires the small-scale convection pattern, which can be achieved only with low viscosity. Thus we use the radiative diffusivity to decrease the Rossby number in the convection zone until an acceleration of the equator is reproduced. We implicitly assume that the numerically unresolved thermal convection transports substantial energy in the real Sun. We note that both high resolution and higher position of the top boundary make it difficult to obtain the accelerated equator, since both increase the Rossby number and are likely breaking coherent rotationally aligned flows (“banana cells”). Thus a rather severe measure is required, i.e., 18 times smaller luminosity, for achieving a faster rotating equator in

this study. While our setup allows us to generate self-consistently a solar-like differential rotation and a near surface shear layer, we have to be careful when applying our result to the Sun. The resolution is  $384(N_r) \times 648(N_\theta) \times 1944(N_\phi) \times 2$  in the Yin-Yang grid, which is fairly high compared to other calculation (e.g., Miesch et al. 2008) except for that in Paper I. The top and bottom boundaries are at  $0.99R_\odot$  and  $0.715R_\odot$ , respectively. Both boundaries are impenetrable and stress free, i.e.,  $v_r = \partial(v_\theta/r)/\partial r = \partial(v_\phi/r)/\partial r = 0$ . A free boundary condition (zero gradient) is adopted for the density and entropy perturbation ( $\partial\rho_1/\partial r = \partial s_1/\partial r = 0$ ).

### 3. Result

We use previously calculated data using higher artificial viscosity and old expression of the RSST, i.e., using  $\rho_0$  instead of  $\rho$ , for 4500 days as a initial condition. Then we switch the expression to current equations (eq. (5)-(7)) and reduce the artificial viscosity and calculate it for 200 days. Since the changes of differential rotation and meridional flow are not so significant, 200 days calculations are enough for the differential rotation and the meridional flow to reach steady state, in which the time derivative of these large-scale flows are small compared with the other terms. In order to analyze the data, we continue the simulation for another 200 days. Fig. 4a shows the temporal evolution of the total energy of the differential rotation ( $\langle v_\phi \rangle$ : black) and the meridional flow ( $\langle v_r \rangle$ : blue and  $\langle v_\theta \rangle$ : red). The temporal evolution of total kinetic energy (black) and total energy from  $t = 0$  are shown in Fig. 4b. Since the plots of the energy (Fig. 4b) indicate long term evolution, we also consider the influence of this evolution with estimating  $\partial\langle\mathcal{L}\rangle/\partial t$  and  $\partial\langle\omega_\phi\rangle/\partial t$  in the following analyses. Rather large time evolution is seen in the total energy  $\rho e_1 + \rho v^2/2$  (red line in Fig. 4). We confirmed that this can be mostly explained with the imbalance of the energy flux between the bottom and the top boundary caused by artificial viscosity



on the entropy and the radiative diffusion. This can be fixed in the future study. This imbalance corresponds to about 3% of the convective energy flux through the system and potentially influences results on this level. The conservation of the angular momentum is reasonably confirmed in this period (Figs. 4c). RMS values of the density, the pressure and the entropy are shown in Fig. 5. These values are normalized by the background values in order to show the validity of the linearized equation of state (eq. (8)). The dotted line shows the distribution of  $\xi^2[\rho_1/\rho_0]_{\text{RMS}}$ . Since  $\xi^2\rho_1/\rho_0$  is 0.023 at maximum, it does not influence our analyses by taking  $\rho_0$  instead of  $\rho = \rho_0 + \xi^2\rho_1$  and we mention this issue again in the following analyses. We note that since we do not use  $\xi^2\rho_1$  but  $\rho_1$  for the equation of state, the linearization of the equation of state is valid. To increase the statistical validity, we average the north and south hemispheres considering the symmetry. Fig. 6 shows the snapshot of the radial velocity  $v_r$  at  $t = 200$  day at selected depth, where  $t = 0$  is the start of the analysis. (The corresponding movie is available online.) The white lines show the location of the tangential cylinder  $r \sin \theta = r_{\text{min}}$ . We can reproduce 10 Mm scale convection at  $r = 0.99R_\odot$  without any influence of the rotation in which we cannot see any clear alignment of the convection pattern along the rotational axis (the banana cell). At  $r = 0.92R_\odot$ , the banana cell like feature begins to appear and at  $r = 0.85R_\odot$ , we can see clear banana cell pattern. In addition, the banana cell pattern is seen outside the tangential cylinder. This dependence of the convection pattern on the depth is basically determined by the Rossby number. Figs. 7a and b show the radial profile of RMS velocity and the Rossby number defined here by  $\text{Ro} = v_{\text{RMS}}/(2\Omega_0 H_p)$ , respectively. Three components of the RMS velocity monotonically increase along with radius, whereas  $v_r$  monotonically decreases above  $0.975R_\odot$  due to the top boundary condition. The Mach number defined with RMS velocity and the reduced speed of sound is 0.12 at maximum. This satisfies the criterion obtained in Hotta et al. (2012b). This and the decrease in the pressure scale height  $H_p$  cause the significant increase of the Rossby number around the surface. Especially above

$r = 0.93R_{\odot}$ , the Rossby number exceeds unity indicating weak rotational influence on the convective flow.

Fig. 8 shows the distribution of the angular velocity ( $\langle\Omega\rangle/(2\pi)$ ), where  $\Omega = \Omega_0 + \Omega_1$  and  $\Omega_1 = v_{\phi}/(r \sin \theta)$ . The NSSL's features are clearly seen especially in the low colatitude ( $\theta > 45$  degree) and high colatitude ( $\theta < 30$  degree). We note that mid-colatitude is where poleward meridional flow is most efficient at maintaining the Taylor-Proudman state, i.e., hardest to maintain NSSL (see also Guerrero et al. 2013). In the convection zone at the low to mid latitude, the differential rotation is almost in the Taylor-Proudman state ( $\partial\langle\Omega\rangle/\partial z \sim 0$ ). Note that the angular velocity has similar values to the solar one, i.e., 460 nHz and 340 nHz at the equator and the polar regions, respectively. Fig. 9 shows the radial profile of the angular velocity at selected colatitude. At low colatitude ( $\theta = 30$  and 45 degree), we can clearly see the decrease of the angular velocity from  $r = 0.95R_{\odot}$  to  $0.975R_{\odot}$ , which is the feature of the NSSL. At the mid colatitude  $\theta = 60$  degrees the tendency is reversed. The angular velocity increases more steeply than that in the deep convection zone. At the high colatitude, the decrease from  $r = 0.92R_{\odot}$  to  $0.99R_{\odot}$  is seen. The sign change of  $\partial\Omega/\partial r$  above  $0.975R_{\odot}$  is related to the influence from the top boundary causing the RMS value of  $v_r$  to drop significantly.

Fig. 10 shows the mean meridional flow. Fig. 10b clearly shows that in the near surface area ( $> 0.9R_{\odot}$ ), there is prominent poleward flow which is caused by the radially inward angular momentum transport. An equatorward directed meridional flow is found near the base of the convection zone and also in a thin layer round  $0.85 - 0.9 R_{\odot}$  below 45 deg latitude. In the convection zone, the multi-cell structure of the meridional flow is generated, which is on qualitative level similar to the recent finding by the local helioseismology (Zhao et al. 2013).

From our equation of motion, the balance equation for the specific angular momentum

is expressed as

$$\frac{\partial \langle \mathcal{L} \rangle}{\partial t} = -\langle \mathbf{v}_m \rangle \cdot \nabla \langle \mathcal{L} \rangle - \langle (\mathbf{v}'_m \cdot \nabla) \mathcal{L}' \rangle - r \sin \theta \left\langle \frac{\nabla \cdot \mathbf{F}_{\mathbf{v}_\phi}}{\rho} \right\rangle, \quad (10)$$

where the final term shows the artificial viscosity (see Appendix B). Figs. 11a, b, c, and d show  $\rho_0 \partial \langle \mathcal{L} \rangle / \partial t$ ,  $\rho_0 \langle \mathbf{v}_m \rangle \cdot \langle \mathcal{L} \rangle$ ,  $-\rho_0 \langle (\mathbf{v}'_m \cdot \nabla) \mathcal{L}' \rangle$  and (d)  $-\rho_0 r \sin \theta \langle \nabla \cdot \mathbf{F}_{\mathbf{v}_\phi} / \rho \rangle$ , respectively. The background density  $\rho_0$  is multiplied to see the balance in the convection zone and the near surface area simultaneously. The balance between angular momentum transports by the mean flow (panel b) and turbulence (panel c) is fairly good. Since the term  $\rho_0 \partial \langle \mathcal{L} \rangle / \partial t$  is small compared with other term, the distribution of angular momentum is almost in steady state. The L2 norm of  $\partial \langle \mathcal{L} \rangle / \partial t$  is 0.04% of the sum of L2 norm of the terms in the right hand of eq. (10). The effect of the artificial viscosity is seen only around the bottom boundary. This would be caused by the thin fast down flow crashing to the bottom wall boundary. In order to have a discussion with the Reynolds stress, we consider the relation

$$\rho(\mathbf{v} \cdot \nabla) \mathcal{L} = \mathcal{L} \nabla \cdot (\rho \mathbf{v}) + \nabla \cdot (\rho \mathbf{v} \mathcal{L}). \quad (11)$$

Figs. 12a and b show  $\langle \mathcal{L} \nabla \cdot (\rho \mathbf{v}) \rangle$  and  $-\nabla \cdot (\rho_0 \langle \mathbf{v}'_m \mathcal{L}' \rangle)$ , respectively. The contribution related to  $\nabla \cdot (\rho \mathbf{v})$  is very small and the values  $-\rho_0 \langle (\mathbf{v}'_m \cdot \nabla) \mathcal{L}' \rangle$  and  $-\nabla \cdot (\rho_0 \langle \mathbf{v}'_m \mathcal{L}' \rangle)$  are almost equivalent. Thus we can use the Reynolds stress, i.e., the correlation of velocities, to understand the balance of angular momentum. We confirmed the relations of  $\xi^2 \langle \rho' \mathbf{v}'_m \mathcal{L}' \rangle \ll \rho_0 \langle \mathbf{v}'_m \mathcal{L}' \rangle$  and  $\xi^2 \langle \rho' \mathbf{v}'_m \rangle \ll \rho_0 \langle \mathbf{v}_m \rangle$ , where  $\rho' = \rho_1 - \langle \rho_1 \rangle$ . Figs. 13a and b show the correlations between the velocities, that is  $\langle v'_r v'_\phi \rangle$  and  $\langle v'_\theta v'_\phi \rangle$ . We note that these correlations are not normalized by the RMS velocity (different from the definition in Paper I). The negative correlation of  $\langle v'_r v'_\phi \rangle$  which is speculated by Fig. 2 is reproduced, which causes the radially inward angular momentum transport. This negative correlation is not confined to the NSSL. In contrast, at low-latitudes, a positive correlation of  $\langle v'_\theta v'_\phi \rangle$  is realized, and is likely due to the banana-cell-like features (Miesch 2005).

As introduced in §1.1, the discussion regarding the meridional force balance is required to understand the maintenance mechanism of the NSSL in addition to the angular momentum transport shown in Fig. 13. We discuss the dynamical balance by using the correlation of velocities. Thus we check the relation of

$$\nabla \times (\langle \mathbf{v} \times \boldsymbol{\omega} \rangle) = -\nabla \times \left[ \left\langle \frac{1}{\rho} (\langle \nabla \cdot (\rho \mathbf{v} \mathbf{v}) - \mathbf{v} \nabla \cdot (\rho \mathbf{v}) \rangle) \right\rangle \right]. \quad (12)$$

Figs. 14a, and c show the first term of the left hand side and the second term of the right hand side, respectively. Fig. 14b shows the value  $\mathcal{C} = -\nabla \times [\nabla \cdot (\rho_0 \langle \mathbf{v} \mathbf{v} \rangle) / \rho_0]$ . Figs. 14a and b are almost equivalent and the value related to  $\nabla \cdot (\rho \mathbf{v})$  is negligible. Thus, we use  $\mathcal{C}$  as the transport term instead of  $\nabla \times (\langle \mathbf{v} \times \boldsymbol{\omega} \rangle)$ . We divide the contribution of the dynamical balance on the meridional plane as:

$$\mathcal{W} - \mathcal{T} = \mathcal{B} + \tilde{\mathcal{C}} + \mathcal{C}' + \mathcal{V}, \quad (13)$$

where

$$\mathcal{W} = \frac{\partial \langle \omega_\phi \rangle}{\partial t}, \quad (14)$$

$$\mathcal{T} = r \sin \theta \frac{\partial \langle \Omega \rangle^2}{\partial z}, \quad (15)$$

$$\mathcal{B} = - \left[ \nabla \times \left( \frac{\nabla p_1 + \rho_1 g \mathbf{e}_r}{\rho} \right) \right]_\phi. \quad (16)$$

The term  $\mathcal{T}$  is caused by the Coriolis force on the meridional plane, which contributes to the balance when the differential rotation deviates from the Taylor-Proudman state ( $\partial \langle \Omega \rangle / \partial z \neq 0$ ). The term  $\mathcal{B}$  is caused by the pressure gradient and the buoyancy (baroclinic term) and requires a latitudinal entropy gradient to be present. The detailed form of  $\mathcal{C}'$  and  $\tilde{\mathcal{C}}$  are found in the Appendix C. These two are caused by the momentum transport within the meridional plane.  $\mathcal{C}'$  and  $\tilde{\mathcal{C}}$  are contribution by the mean meridional flow ( $\langle v_r \rangle$  and  $\langle v_\theta \rangle$ ) and the non-axisymmetric flow ( $v'_r$  and  $v'_\theta$ ), respectively.  $\mathcal{V}$  is contribution from the artificial viscosity (see Appendix B and C). Fig. 15 shows the distribution of (a)  $\mathcal{W}$ , (b)  $-\mathcal{T}$ , (c)  $\mathcal{B}$ ,

(d)  $\tilde{\mathcal{C}}$ , (e)  $\mathcal{C}'$ , and (f)  $\mathcal{V}$ . According to the distribution of the  $-\mathcal{T}$ , we divide the meridional plane to four regions (I, II, III, and IV as shown in Fig. 15b). Region I is the maintained by the latitudinal entropy gradient  $\mathcal{B}$  from the middle to the bottom of the convection zone. In the other regions (II, III, and IV), the deviation from the Taylor-Proudman state cannot be explained by the entropy gradient alone. The contributions from time evolution  $\mathcal{W}$  (panel a), mean flow  $\tilde{\mathcal{C}}$  (panel d), and artificial viscosity  $\mathcal{V}$  (panel f) have negligible role even in the NSSL. Then we see that the contribution from the non-axisymmetric flow ( $\mathcal{C}'$ : Fig. 15d) is almost totally compensates the term  $-\mathcal{T}$  at the regions II, III, and IV. To investigate the origin of the distribution of  $\mathcal{C}'$ , which can maintain the NSSL, we divide the term  $\mathcal{C}'$  to three as  $\mathcal{C}' = \mathcal{C}'_d + \mathcal{C}'_\theta + \mathcal{C}'_r$ . The detailed forms of them are found in the Appendix C. The term  $\mathcal{C}'_d$  is caused by the diagonal momentum flux  $F'_{rr}$ ,  $F'_{\theta\theta}$ , and  $F'_{\phi\phi}$ , where  $F'_{ij} = \rho_0 \langle v'_i v'_j \rangle$  (see Appendix C). The terms  $\mathcal{C}'_\theta$  and  $\mathcal{C}'_r$  are caused by the non-diagonal momentum flux  $F'_{r\theta}$ . The difference of these two terms is explained as: The term  $\mathcal{C}'_\theta$  ( $\mathcal{C}'_r$ ) is caused by the transport of the latitudinal momentum  $\rho_0 v'_\theta$  (radial momentum  $\rho_0 v'_r$ ) in the radial (latitudinal) direction. We note that  $\mathcal{C}'_r$  and  $\mathcal{C}'_\theta$  can act as turbulent diffusivity on meridional flow. Fig. 16 shows the distribution of (a)  $\mathcal{C}'_d$ , (b)  $\mathcal{C}'_\theta$ , and (c)  $\mathcal{C}'_r$ . The diagonal term  $\mathcal{C}'_d$  has contribution to some degree and the contribution from the term  $\mathcal{C}'_r$  is negligible. The essential contribution is by the term  $\mathcal{C}'_\theta$ , i.e., the transport of the latitudinal momentum in the radial direction.

Next we investigate the origin of  $\mathcal{C}'_\theta$  by estimating the quantity  $D'_{\theta(n)}$ , which is latitudinal force arising from momentum transport (see Appendix C for a more complete definition of  $D$ ). This force is defined as

$$D'_{\theta(n)} = -\frac{1}{\rho_0} \left[ \frac{1}{r^2} \frac{\partial}{\partial r} (r^2 F'_{r\theta}) - \frac{F'_{\theta r}}{r} \right], \quad (17)$$

which it is related to  $\mathcal{C}'_\theta$

$$\mathcal{C}'_\theta = \frac{1}{r} \frac{\partial}{\partial r} (r D'_{\theta(n)}), \quad (18)$$

and where the subscript  $\theta(n)$  refers to the inertial force in the latitudinal direction arising from the non-diagonal Reynolds stress  $F'_{r\theta} = \langle v'_r v'_\theta \rangle$ . Fig. 17 shows (a)  $D'_{\theta(n)}$  and (b)  $\langle v'_r v'_\theta \rangle$ , where in (a) it is evident that the direction of the inertial force is equatorward (poleward) at the top (bottom) of the NSSL at high latitudes (i.e., Region II). In this region, the inertial force tends to balance the Coriolis force. The origin of this inertial force is the Reynolds stress  $\langle v'_r v'_\theta \rangle$ , as can be deduced from the correlation of Figs. 17b. In the high-latitude NSSL, the positive correlation  $\langle v'_r v'_\theta \rangle > 0$  leads to the upward transport of latitudinal momentum. In contrast, in the high-latitude deep convection zone, the correlation is negative. This arrangement of momentum flux increases (decreases) the latitudinal momentum in the upper (lower) part of the NSSL (Fig. 17a). These correlations are the essential ingredients that maintain the meridional flow within the NSSL at high latitudes.

The following discussion is centered around the origin of velocity correlations generated from a combination of rotation and large scale shear. We retain the dominant terms that can generate a positive or negative correlation as:

$$\frac{\partial v'_r}{\partial t} = -\frac{v'_\theta}{r} \frac{\partial \langle v_r \rangle}{\partial \theta} + 2v'_\phi \langle \Omega \rangle \sin \theta + [...], \quad (19)$$

$$\frac{\partial v'_\theta}{\partial t} = -v'_r \frac{\partial \langle v_\theta \rangle}{\partial r} + 2v'_\phi \langle \Omega \rangle \cos \theta + [...], \quad (20)$$

$$\frac{\partial v'_\phi}{\partial t} = -2v'_r \langle \Omega \rangle \sin \theta - 2v'_\theta \langle \Omega \rangle \cos \theta + [...]. \quad (21)$$

The sign of velocity correlation significantly depends on whether  $v'_r$  and  $v'_\theta$  is generated by  $v'_\phi$  (Situation 1) or  $v'_\phi$  is generated by  $v'_r$  and  $v'_\theta$  (Situation 2). The signs of  $\langle v'_r v'_\phi \rangle$  and  $\langle v'_\theta v'_\phi \rangle$  are the direct consequence of these situations. When the Situation 1 is achieved, a positive correlations ( $\langle v'_r v'_\phi \rangle$  and  $\langle v'_\theta v'_\phi \rangle$ ) are generated through eqs. (19) and (20). On the other hand, under the Situation 2, a negative correlations are generated through eq. (21). Figs. 13a and b indicate that the Situation 1 requires both the low Rossby number and the banana cell, i.e., deeper layer and outside the tangential cylinder, since the positive

correlations ( $\langle v'_r v'_\phi \rangle$  and  $\langle v'_\theta v'_\phi \rangle$ ) are especially seen there. Outside the tangential cylinder with low Rossby number, the zonal flow  $v'_\phi$  is dominant due to coherent banana cell structure with weak influence from the bottom boundary (Gilman 1979; Miesch et al. 2000; Miesch 2005; Brun et al. 2011). Thus  $v'_\phi$  generates  $v'_r$  and  $v'_\theta$  there. In contrast to the Situation 1, the Situation 2 is realized even in high Rossby number. The role of the meridional flow, however, becomes large in a high Rossby number situation (see the following discussion).

Before discussing the origin of the correlation  $\langle v'_r v'_\theta \rangle$  in the high-latitude NSSL, we first describe the feature found in low latitudes. From the high- to the mid-latitudes we find a negative correlation in the near surface layer, while a positive correlation is generated in the lower latitude from the surface to the middle of the convection zone. This positive correlation is generated by the banana cells. When both the radial and latitudinal velocities are generated by the Coriolis force, the correlation  $\langle v'_r v'_\theta \rangle$  can be positive (see also eq. (19) and (20)). In the NSSL, however, the Rossby number is large and banana cells do not exist. This means that the positive correlation  $\langle v'_r v'_\theta \rangle$  in the high latitude NSSL is generated by different mechanism(s). The first term in each of the eqs. (19) and (20) is that due to the mean meridional flow that is the most important element in this discussion. In this discussion, we focus on the correlation between  $v'_r$  and  $v'_\theta$ . When the typical time scale is estimated as  $\tau = H_p/v_{\text{RMS}}$ , we obtain the relation

$$v'_\phi \sim -2\tau v'_r \langle \Omega \rangle \sin \theta - 2\tau v'_\theta \langle \Omega \rangle \cos \theta, \quad (22)$$

from eq. (21). Note that we can use this transformation, since the region is inside the tangential cylinder where no banana cell exists and  $v'_\phi$  is generated by  $v'_r$  and  $v'_\theta$  (see the discussion in previous paragraph). We substitute this relation to eqs. (19) and (20) and only retain the terms that can generate the nonzero correlation between  $v'_r$  and  $v'_\theta$ :

$$\frac{\partial v'_r}{\partial t} = [\dots] - \frac{v'_\theta}{r} \frac{\partial \langle v_r \rangle}{\partial \theta} - 2v'_\theta \tau \langle \Omega \rangle^2 \sin(2\theta), \quad (23)$$

$$\frac{\partial v'_\theta}{\partial t} = [\dots] - v'_r \frac{\partial \langle v_\theta \rangle}{\partial r} - 2v'_r \tau \langle \Omega \rangle^2 \sin(2\theta), \quad (24)$$

This means that the terms from the Coriolis force (i.e., the last term in each equation) generates a negative correlation between  $v'_r$  and  $v'_\theta$ . This is expected since a strong Coriolis force leads to fluid motions preferentially aligned with the axis of rotation. The sign of the correlation by the mean flow depends on the sign of  $\partial\langle v_r\rangle/(r\partial\theta)$  and  $\partial\langle v_\theta\rangle/\partial r$ . Fig. 18 shows the distribution of (a)  $\partial\langle v_r\rangle/(r\partial\theta)$ , and (b)  $\partial\langle v_\theta\rangle/\partial r$ . It is clear that the contribution from the term related to  $\partial\langle v_r\rangle/(r\partial\theta)$  is small compared with the term of  $\partial\langle v_\theta\rangle/\partial r$ . Interestingly we find a negative value of  $\partial\langle v_\theta\rangle/\partial r$  in region II and a positive value in region IV. Only when  $\partial\langle v_\theta\rangle/\partial r$  is negative, the correlation  $\langle v'_r v'_\theta \rangle$  can have a positive value. On the contrary there is negative  $\langle v'_r v'_\theta \rangle$  in region IV with positive  $\partial\langle v_\theta\rangle/\partial\theta$  (see Fig. 18b).

The effectiveness of the generation of the positive correlation by the mean meridional flow can be estimated as follows:

$$\mathcal{M} = -\frac{\partial\langle v_\theta\rangle/\partial r}{2\tau\langle\Omega\rangle^2\sin(2\theta)} \sim -\frac{1}{\sin(2\theta)\langle\Omega\rangle} \frac{\partial\langle v_\theta\rangle}{\partial r} \overline{\text{Ro}}, \quad (25)$$

where  $\overline{\text{Ro}} = v_{\text{rms}}/(2\langle\Omega\rangle H_p)$ . When  $\mathcal{M}$  is larger than unity, the meridional flow is effective in generating the correlation  $\langle v'_r v'_\theta \rangle$ . We note that the mathematical form of  $\mathcal{M}$  indicates that it is most difficult to achieve this balance in mid-latitude due to the factor of  $1/\sin(2\theta)$ , assuming the meridional flow is the same at all latitudes. Since the positive correlation is found in between  $\theta = 20$  and  $40$  degrees, we estimate  $\sin(2\theta) \sim 0.5$ . Using the values  $\langle\Omega\rangle/(2\pi) = 380$  nHz,  $\overline{\text{Ro}} = v_{\text{RMS}}/(2\langle\Omega\rangle H_p) \sim 3$  (which is taken from Fig. 7 at the base of the NSSL) and  $\partial\langle v_\theta\rangle/\partial r \sim -4 \times 10^{-7} \text{ s}^{-1}$  (around  $r = 0.95R_\odot$ ), leads to a value of  $\mathcal{M}$  at the base of NSSL of 1. This shows that the generation of the positive correlation by the mean poleward flow begins to be effective in the base of the NSSL. When the value  $\partial\langle v_\theta\rangle/\partial r$  is positive both terms of the meridional flow and the Coriolis force generate a negative correlation. This cannot generate the solar-like NSSL even under the large Rossby number situation (region IV).



In the low latitude NSSL (region III), the positive correlation  $\langle v'_r v'_\theta \rangle$  is mostly generated by the banana cell convection with some contribution from the poleward meridional flow, where  $\partial \langle v_\theta \rangle / \partial r < 0$  (Fig. 17b). Around the tangential cylinder (white line) the effect of the banana cells and the meridional flow is ineffective and the correlation  $\langle v'_r v'_\theta \rangle$  is negative. In the boundary of the effective and ineffective layer of these mechanisms i.e. the boundary of the positive and negative correlation  $\langle v'_r v'_\theta \rangle$ , the fluid is accelerated poleward due to inertial force, which compensates the Coriolis force in the low latitude NSSL. The circle in Fig. 17 indicates the boundary area which has poleward acceleration.

In this study, the equatorward meridional flow in the very near surface is generated. Although the origin of the equatorward meridional flow is unknown, this type of feature is seen in the previous study (Miesch et al. 2008). We find that the equatorward meridional flow is generated in the region where the inward directed transport stops. This means the angular momentum is deposited in this region by the Reynolds stress, which will be transported by the equatorward meridional flow. Although in current global calculation we must have thick cooling layer ( $\sim 4000$  km), in which the radial velocity and its radially inward angular momentum transport decrease, the real sun has much thinner one ( $\sim 100$  km) in the photosphere. The real solar situation might not cause a sign change of  $d \langle v_\theta \rangle / dr$  in the real sun. The distribution of the NSSL especially in the low latitude should be confirmed with higher-resolution in the future.

#### 4. Summary and Discussion

We presented a high-resolution, highly stratified numerical simulation of rotating thermal convection in a spherical shell. We find the self-consistent generation of a NSSL mostly in high latitudes and analyzed in detail the underlying angular momentum transport terms and meridional force balance.

With regard to the angular momentum transport, the maintenance mechanism is the same as that suggested by Foukal & Jokipii (1975) and Gilman & Foukal (1979). Convection with small rotational influence leads to radially inward transport of angular momentum. Since the NSSL deviates significantly from the Taylor-Proudman state ( $\partial\langle\Omega_1\rangle/\partial z \neq 0$ ), mechanisms are required to balance the Coriolis force which tends to drive the NSSL towards the Taylor-Proudman state. These are related to velocity correlations (Reynolds-stresses) within the meridional plane.

Fig. 19a summarizes the distribution of the correlations. In the high latitude NSSL, a positive correlation  $\langle v'_r v'_\theta \rangle$  is generated by the poleward meridional with negative radial gradient ( $\partial\langle v_\theta \rangle/\partial r < 0$ ). This can be interpreted as a turbulent viscous stress  $-\nu_t r \partial(\langle v_\theta \rangle/r)/\partial r$  in near surface layer. The distribution of estimated turbulent viscosity stress is shown in Fig. 20, where the turbulent viscosity is estimated as  $\nu_t = v_{\text{RMS}} H_p/3$  (Hotta et al. 2012a).

Fig. 19b summarizes the dynamical balance on the meridional plane. The poleward meridional flow is generated due to the inward angular momentum transport. This flow grows until a combination of turbulent viscous stress and acceleration forces can balance the Coriolis force. The reason this works in the NSSL is that the radial gradient of the meridional flow ( $d\langle v_\theta \rangle/dr$ ) is strong and the RMS velocity is large.

We note that there were some studies that tried to explain differential rotation through turbulent viscous stresses. This, however, requires, significantly larger Rossby number, i.e., smaller Taylor number, than that expected in the solar convection zone (Brandenburg et al. 1990; Kitchatinov & Rüdiger 1995; Williams 2006), which was phrased the “Taylor-number puzzle” in the literature. In this study, this balance between the Coriolis force and the inertial force is well achieved in the high latitude. In the low latitude, the banana cell generates the positive correlation which increases along the radius and accelerates the fluid

poleward (region III: around the tangential cylinder which is highlighted by circle in Fig. 17). When the equatorward meridional flow with increasing amplitude ( $\partial\langle v_\theta\rangle/\partial r > 0$ ) is effective, i.e., the large Rossby number, the correlation  $\langle v'_r v'_\theta \rangle$  becomes negative (region IV). At the layer where this effect begins to occur, the fluid is accelerated equatorward. Then, the negative correlation becomes zero with approaching the boundary, which then accelerates the fluid poleward again. This complicated transport of momentum governs the meridional force balance of the NSSL at low latitudes.

In this study, we reduced the solar luminosity to obtain the accelerated equator. This reduces the convective velocity and the Rossby number. Thus the profile of the NSSL may be also influenced by the small Rossby number compared with the actual Sun.

The most important findings in this study are that the angular momentum is transported radially inward in the NSSL and that the turbulent viscous stress resulting from the radial gradient of the latitudinal meridional flow, i.e.,  $\nu_t r \partial(\langle v_\theta \rangle / r) \partial r$ , plays an essential role for the maintenance of the NSSL.

Our difficulties in obtaining a solar-like profile of the NSSL in very near surface layer are possibly related to the top boundary condition which forces  $v_r$  to go to zero. Observations (Zhao et al. 2013) indicate a poleward flow with increasing amplitude in radius, which would lead to the proper positive correlation  $\langle v'_r v'_\theta \rangle$  required for a solar-like NSSL.

We are grateful to anonymous referee for the helpful comments and leading us to find the new expression of the RSST. H. H. is supported by Grant-in-Aid for JSPS Fellows. The National Center for Atmospheric Research is sponsored by the National Science Foundation. The results are obtained by using K computer at the RIKEN Advanced Institute for Computational Science (Proposal number hp130026 and hp140212). This work

was supported in part by MEXT SPIRE and JICFuS. The authors are grateful to Rachel Howe for giving us the HMI inversion data. In particular, the authors thank Mark Miesch for educating us about the role of the gyroscopic pumping and the meridional force balance and giving us the insightful comments on the manuscript.

## REFERENCES

- Balbus, S. A. 2009, MNRAS, 395, 2056
- Brandenburg, A. 2007, in IAU Symposium, Vol. 239, IAU Symposium, ed. F. Kupka, I. Roxburgh, & K. L. Chan, 457–466
- Brandenburg, A., Tuominen, I., Moss, D., & Ruediger, G. 1990, Sol. Phys., 128, 243
- Brun, A. S., Miesch, M. S., & Toomre, J. 2011, ApJ, 742, 79
- Christensen-Dalsgaard, J., et al. 1996, Science, 272, 1286
- De Rosa, M. L., Gilman, P. A., & Toomre, J. 2002, ApJ, 581, 1356
- Fan, Y., Featherstone, N., & Fang, F. 2013, ArXiv e-prints
- Foukal, P., & Jokipii, J. R. 1975, ApJ, 199, L71
- Gastine, T., Yadav, R. K., Morin, J., Reiners, A., & Wicht, J. 2014, MNRAS, 438, L76
- Gilman, P. A. 1979, ApJ, 231, 284
- Gilman, P. A., & Foukal, P. V. 1979, ApJ, 229, 1179
- Guerrero, G., Smolarkiewicz, P. K., Kosovichev, A., & Mansour, N. 2013, in IAU Symposium, Vol. 294, IAU Symposium, ed. A. G. Kosovichev, E. de Gouveia Dal Pino, & Y. Yan, 417–425
- Hotta, H., Iida, Y., & Yokoyama, T. 2012a, ApJ, 751, L9
- Hotta, H., Rempel, M., & Yokoyama, T. 2014, ApJ, 786, 24
- Hotta, H., Rempel, M., Yokoyama, T., Iida, Y., & Fan, Y. 2012b, A&A, 539, A30
- Hotta, H., & Yokoyama, T. 2011, ApJ, 740, 12

- Howard, R., Gilman, P. I., & Gilman, P. A. 1984, *ApJ*, 283, 373
- Howe, R. 2009, *Living Reviews in Solar Physics*, 6, 1
- Howe, R., Larson, T. P., Schou, J., Hill, F., Komm, R., Christensen-Dalsgaard, J., & Thompson, M. J. 2011, *Journal of Physics Conference Series*, 271, 012061
- Käpylä, P. J., Mantere, M. J., Guerrero, G., Brandenburg, A., & Chatterjee, P. 2011, *A&A*, 531, A162
- Kitchatinov, L. L., & Rüdiger, G. 1995, *A&A*, 299, 446
- Matt, S. P., Do Cao, O., Brown, B. P., & Brun, A. S. 2011, *Astronomische Nachrichten*, 332, 897
- Miesch, M. S. 2005, *Living Reviews in Solar Physics*, 2, 1
- Miesch, M. S., Brun, A. S., De Rosa, M. L., & Toomre, J. 2008, *ApJ*, 673, 557
- Miesch, M. S., Brun, A. S., & Toomre, J. 2006, *ApJ*, 641, 618
- Miesch, M. S., Elliott, J. R., Toomre, J., Clune, T. L., Glatzmaier, G. A., & Gilman, P. A. 2000, *ApJ*, 532, 593
- Miesch, M. S., & Hindman, B. W. 2011, *ApJ*, 743, 79
- Mihalas, D., & Mihalas, B. W. 1984, *Foundations of radiation hydrodynamics*
- Rast, M. P., Ortiz, A., & Meisner, R. W. 2008, *ApJ*, 673, 1209
- Rempel, M. 2005, *ApJ*, 622, 1320
- . 2014, *ApJ*, 789, 132

- Thompson, M. J., Christensen-Dalsgaard, J., Miesch, M. S., & Toomre, J. 2003, *ARA&A*, 41, 599
- Williams, P. T. 2006, in *Astronomical Society of the Pacific Conference Series*, Vol. 354, *Solar MHD Theory and Observations: A High Spatial Resolution Perspective*, ed. J. Leibacher, R. F. Stein, & H. Uitenbroek, 85
- Zhao, J., Bogart, R. S., Kosovichev, A. G., Duvall, Jr., T. L., & Hartlep, T. 2013, *ApJ*, 774, L29

### A. New expression of RSST

As explained in Paper I, using the original RSST form the momentum and the total energy are not conserved. In this paper, we adopt the new expression of the RSST in which these values are mathematically conserved. The conserved value related to the total energy is  $\rho T s_1 + \rho v^2/2$  and this requires linear approximation. Our approach is summarized as: 1. the total density is expressed as  $\rho = \rho_0 + \tilde{\rho}_1$ . 2. using the ordinary linearized equations of continuity, motion and state with reducing the adiabatic speed of sound and the buoyancy term as:

$$\frac{\partial \tilde{\rho}_1}{\partial t} = -\nabla \cdot (\rho \mathbf{v}), \quad (\text{A1})$$

$$\rho \frac{\partial \mathbf{v}}{\partial t} = -\rho (\mathbf{v} \cdot \nabla) \mathbf{v} - \nabla p_1 - \frac{\tilde{\rho}_1}{\xi^2} g \mathbf{e}_r + [\dots], \quad (\text{A2})$$

$$p_1 = \left( \frac{\partial p}{\partial \rho} \right)_s \frac{\tilde{\rho}_1}{\xi^2} + \left( \frac{\partial p}{\partial s} \right)_\rho s_1. \quad (\text{A3})$$

In this idea, we simply reduce the adiabatic speed of sound  $(\partial p / \partial \rho)_s$  by factor of  $\xi^2$  with eq. (A3). The balance in the equation of motion makes the perturbation of the pressure same. This causes the increase of the density perturbation  $\tilde{\rho}_1$  by factor of  $\xi^2$ . In order to avoid the increase of the buoyancy, i.e., to keep the proper balance between pressure gradient and buoyancy, the density perturbation for the buoyancy is divided by  $\xi^2$  (eq. (A2)). We tested the validity of this method using a similar way to Hotta et al. (2012b), i.e., a Cartesian box test problem. We confirm that with the reduction of the adiabatic speed of sound scales up the density perturbation by the factor of  $\xi^2$  with remaining the shape of the RMS and mean density. Tilde is used, since  $\tilde{\rho}_1$  is increased from the ordinary density perturbation  $\rho_1$  by the factor of  $\xi^2$ .

Since the quantity  $\tilde{\rho}_1 / \xi^2$  remains invariant in leading order when changing  $\xi$ , it is more convenient to write  $\rho = \rho_0 + \xi^2 \rho_1$ . Using this expression for the density, we can derive a



form of the RSST that is similar to (Hotta et al. 2012b),

$$\frac{\partial \rho}{\partial t} = -\nabla \cdot (\rho \mathbf{v}) \rightarrow \frac{\partial \rho_1}{\partial t} = -\frac{1}{\xi^2} \nabla \cdot (\rho \mathbf{v}). \quad (\text{A4})$$

We note that we use  $\rho$  instead of  $\rho_0$  in right hand side. In addition, we also use  $\rho$  for the equation of motion and entropy as:

$$\rho \frac{\partial \mathbf{v}}{\partial t} = -\rho(\mathbf{v} \cdot \nabla) \mathbf{v} - \nabla p_1 - \rho_1 g \mathbf{e}_r + [...], \quad (\text{A5})$$

$$\rho T \frac{\partial s_1}{\partial t} = -\rho T(\mathbf{v} \cdot \nabla) s_1 + [...]. \quad (\text{A6})$$

The equation of state is expressed as:

$$p_1 = \left( \frac{\partial p}{\partial s} \right)_s \rho_1 + \left( \frac{\partial p}{\partial \rho} \right)_\rho s_1. \quad (\text{A7})$$

Then the variable  $\rho$  is conserved mathematically. We again note that in this discussion  $\rho = \rho_0 + \xi^2 \rho_1$ . In addition, the expressions

$$\rho \frac{\partial \mathbf{v}}{\partial t} + \rho(\mathbf{v} \cdot \nabla) \mathbf{v}, \quad (\text{A8})$$

and

$$\frac{\partial}{\partial t}(\rho \mathbf{v}) + \nabla \cdot (\rho \mathbf{v} \mathbf{v}), \quad (\text{A9})$$

are identical. This means that the angular momentum  $\rho \mathcal{L}$  is conserved with this form mathematically.

Next, we derive the conservation of total energy under the linear approximation, i.e., ignore the second order term. From the hydrostatic equilibrium, the relation

$$\begin{aligned} g &= -\frac{1}{\rho_0} \frac{dp_0}{dr} \\ &= -\frac{1}{\rho_0 v_r} \frac{Dp_0}{Dt}, \end{aligned} \quad (\text{A10})$$

is obtained, where  $D/Dt = \partial/\partial t + \mathbf{v} \cdot \nabla$  is the Lagrangian derivative. The equation of the kinetic energy is written as:

$$\begin{aligned} \rho \frac{D}{Dt} \left( \frac{1}{2} v^2 \right) + (\mathbf{v} \cdot \nabla) p_1 + v_r \rho_1 g &= \rho \frac{D}{Dt} \left( \frac{1}{2} v^2 \right) \\ &+ \nabla \cdot (\mathbf{v} p_1) + \frac{p_1}{\rho} \frac{D\rho}{Dt} - \frac{\rho_1}{\rho_0} \frac{Dp_0}{Dt} \\ &= 0. \end{aligned} \quad (\text{A11})$$

Our background temperature gradient is adiabatic:

$$s_1 \frac{DT}{Dt} \sim s_1 \frac{DT_0}{Dt} = s_1 \left( \frac{\partial T}{\partial \rho} \right)_s \frac{D\rho_0}{Dt} \quad (\text{A12})$$

$$= s_1 \left( \frac{\partial T}{\partial p} \right)_s \frac{Dp_0}{Dt}. \quad (\text{A13})$$

Then the equation of entropy ( $\rho T Ds_1/Dt = Q$ , where  $Q$  includes radiative diffusion and surface cooling), is transformed as:

$$\begin{aligned} \rho \frac{D}{Dt} (Ts_1) - \rho s_1 \frac{DT}{Dt} &\sim \rho \frac{D}{Dt} (Ts_1) - \rho \left[ \left( \frac{\partial s}{\partial \rho} \right)_p \rho_1 + \left( \frac{\partial s}{\partial p} \right)_\rho p_1 \right] \frac{DT_0}{Dt} \\ &= \rho \frac{D}{Dt} (Ts_1) - \rho \left[ \left( \frac{\partial s}{\partial \rho} \right)_p \left( \frac{\partial T}{\partial p} \right)_s \rho_1 \frac{Dp_0}{Dt} + \left( \frac{\partial s}{\partial p} \right)_\rho \left( \frac{\partial T}{\partial \rho} \right)_s p_1 \frac{D\rho_0}{Dt} \right] \\ &= \rho \frac{D}{Dt} (Ts_1) - \rho \left[ \left( -\frac{c_p}{\beta \rho_0 T_0} \right) \left( \frac{\beta T_0}{c_p \rho_0} \right) \rho_1 \frac{Dp_0}{Dt} + \left( \frac{\kappa_T c_v}{\beta T_0} \right) \left( \frac{\beta T_0}{c_v \kappa_T \rho_0^2} \right) p_1 \frac{D\rho_0}{Dt} \right] \\ &= \rho \frac{D}{Dt} (Ts_1) - \rho \left( -\frac{\rho_1}{\rho_0^2} \frac{Dp_0}{Dt} + \frac{p_1}{\rho_0^2} \frac{D\rho_0}{Dt} \right) = Q, \end{aligned} \quad (\text{A14})$$

where  $\beta$  and  $\kappa_T$  are the coefficient of thermal expansion and the coefficient of isothermal compressibility, respectively (Hotta et al. 2014; Mihalas & Mihalas 1984). Thus the equation of the total energy is expressed with using the linear approximation

$$\rho \frac{D}{Dt} \left( Ts_1 + \frac{1}{2} v^2 \right) + \nabla \cdot (\mathbf{v} p_1) = Q. \quad (\text{A15})$$

The value  $\rho Ts_1 + \rho v^2/2$  is conserved. We note the deviation is mainly caused by the value  $\xi^2 \rho_1/\rho_0$ . Using the equation of state for the perfect gas, the value is transformed as

$\rho T s_1 \sim \rho c_v T_1 - p_0 \rho_1 / \rho_0$ , which means the internal energy and contribution of the buoyancy. We note that using the anelastic approximation ( $0 = \nabla \cdot (\rho_0 \mathbf{v})$ ), the value  $\rho_0 T_0 s_1 + \rho_0 v^2 / 2$  is conserved without any linear approximation. The above derivation assumes the adiabatic background stratification. Some additional terms and assumptions would be required when we have non-adiabatic background stratification

## B. Artificial viscosity

The same artificial viscosity as MuRAM code (Rempel 2014) is added on all the variables as:

$$\frac{\partial}{\partial t}(\rho_1 \xi^2) = -\nabla \cdot \mathbf{F}_\rho, \quad (\text{B1})$$

$$\rho \frac{\partial v_r}{\partial t} = -\nabla \cdot \mathbf{F}_{\mathbf{v}_r}, \quad (\text{B2})$$

$$\rho \frac{\partial v_\theta}{\partial t} = -\nabla \cdot \mathbf{F}_{\mathbf{v}_\theta}, \quad (\text{B3})$$

$$\rho \frac{\partial v_\phi}{\partial t} = -\nabla \cdot \mathbf{F}_{\mathbf{v}_\phi}, \quad (\text{B4})$$

$$\rho T \frac{\partial s_1}{\partial t} = -\nabla \cdot \mathbf{F}_s. \quad (\text{B5})$$

$$F_{i+1/2} = -\frac{1}{2} c_{i+1/2} \phi_{i+1/2} (u_r - u_l, u_{i+1} - u_i) (u_r - u_l), \quad (\text{B6})$$

$$\phi = \begin{cases} \max \left[ 0, 1 + h \left( \frac{u_r - u_l}{u_{i+1} - u_i} - 1 \right) \right] & \text{for } (u_r - u_l) \cdot (u_{i+1} - u_i) > 0, \\ 0 & \text{for } (u_r - u_l) \cdot (u_{i+1} - u_i) \leq 0, \end{cases} \quad (\text{B7})$$

where  $c_{i+1/2} = 0.3c_s + v$  is the characteristic velocity which is the sum of the speed of sound ( $c_s$ ) and fluid velocity ( $v$ ). To decrease the effect of viscosity, a multiplier 0.3 is used and  $h=0.75$  is adopted. In the code, the physical variables  $u_i$  are defined at the center of the cell. To calculate the diffusive flux, the variables  $u_r$  and  $u_l$  at a boundary of the cells are

defined as:

$$u_l = u_i + \frac{1}{2}\Delta u_i, \quad (\text{B8})$$

$$u_r = u_{i+1} - \frac{1}{2}\Delta u_{i+1}, \quad (\text{B9})$$

where the tilt of the variable ( $\Delta u_i$ ) is defined as:

$$\Delta u_i = \text{minimod} \left( \epsilon(u_{i+1} - u_i), \frac{u_{i+1} - u_{i-1}}{2}, \epsilon(u_i - u_{i-1}) \right), \quad (\text{B10})$$

where  $\epsilon$  is the factor for the minimod function ( $1 < \epsilon < 2$ ), in this study  $\epsilon = 1.4$  is used. To conserve total energy, the heat from the dissipated kinetic energy is treated accordingly.

The heat caused by the artificial viscosity is estimated and added in the equation of entropy as

$$\rho T \frac{\partial s_1}{\partial t} = -(\mathbf{F}_r \cdot \nabla)v_r - (\mathbf{F}_\theta \cdot \nabla)v_\theta - (\mathbf{F}_\phi \cdot \nabla)v_\phi. \quad (\text{B11})$$

### C. Dynamical balance on the meridional plane

In the appendix, we derive the equations for the dynamical balance on the meridional plane. We start with the hydrodynamic equation with the Coriolis force used in this paper (eq. (6))

$$\frac{\partial \mathbf{v}}{\partial t} = -(\mathbf{v} \cdot \nabla)\mathbf{v} - \frac{\nabla p_1 + \rho_1 g \mathbf{e}_r}{\rho} + 2\mathbf{v} \times \boldsymbol{\Omega}_0 + \mathbf{G}, \quad (\text{C1})$$

where final term shows the artificial viscosity  $\mathbf{G} = -(\nabla \cdot \mathbf{F}_{\mathbf{v}_r})\mathbf{e}_r - (\nabla \cdot \mathbf{F}_{\mathbf{v}_\theta})\mathbf{e}_\theta - (\nabla \cdot \mathbf{F}_{\mathbf{v}_\phi})\mathbf{e}_\phi$  (see Appendix B). The curl of the first term in the right hand side of eq. (C1) is transformed as  $\nabla \times (\mathbf{v} \times \boldsymbol{\omega})$  with using the vector formula

$$(\mathbf{v} \cdot \nabla)\mathbf{v} = \nabla \left( \frac{v^2}{2} \right) - \mathbf{v} \times (\nabla \times \mathbf{v}). \quad (\text{C2})$$

Although in this paper, we directly take the curl of the second term, it is useful to show the zonal component of the curl of the second term in the right hand side of eq. (C1) with

using  $\rho_0$  instead of  $\rho$  as:

$$\begin{aligned}
\left[ \nabla \times \left( -\frac{\nabla p_1 + \rho_1 g \mathbf{e}_r}{\rho_0} \right) \right]_\phi &= \frac{1}{\rho_0^2 r} \frac{d\rho_0}{dr} \frac{\partial p_1}{\partial \theta} + \frac{g}{\rho_0 r} \frac{\partial \rho_1}{\partial \theta} \\
&= -\frac{g}{\rho_0 r} \left[ \left( \frac{\partial \rho}{\partial p} \right)_s \frac{\partial p_1}{\partial \theta} - \frac{\partial \rho_1}{\partial \theta} \right] \\
&= \frac{g}{\rho_0 r} \left( \frac{\partial \rho}{\partial s} \right)_p \frac{\partial s_1}{\partial \theta},
\end{aligned} \tag{C3}$$

We note that for the perfect gas the value  $(\partial \rho / \partial s)_p = -\rho_0 / c_p$ , where  $c_p$  is the heat capacity at constant volume. Next, the zonal component of the curl of the third term in the left hand side of eq. (C1) is transformed as:

$$\begin{aligned}
\mathcal{T}_0 = [\nabla \times (2\mathbf{v} \times \boldsymbol{\Omega}_0)]_\phi &= [2(\boldsymbol{\Omega}_0 \cdot \nabla) \mathbf{v}_r - 2(\mathbf{v} \cdot \nabla) \boldsymbol{\Omega}_0]_\phi \\
&= 2(\boldsymbol{\Omega}_0 \cdot \nabla) v_\phi = 2r \sin \theta \Omega_0 \frac{\partial \Omega_1}{\partial z},
\end{aligned} \tag{C4}$$

where  $\Omega_1 = v_\phi / (r \sin \theta)$ . In the transformation, the formulation  $\nabla \cdot \boldsymbol{\Omega}_0 = 0$ ,  $\boldsymbol{\Omega}_0 \cdot \mathbf{e}_\phi = 0$ , are used. Fig. 14 shows that the values  $[\nabla \times (\langle \mathbf{v} \times \boldsymbol{\omega} \rangle)]_\phi$  and  $-(\nabla \times [\nabla \cdot (\rho_0 \langle \mathbf{v} \mathbf{v} \rangle) / \rho_0])_\phi$  are almost equivalent and  $\langle \nabla \times (\mathbf{v} / \rho \nabla \cdot (\rho \mathbf{v})) \rangle$  is fairly small compared with the other terms. Thus it is valid to use  $-(\nabla \times [\nabla \cdot (\rho_0 \langle \mathbf{v} \mathbf{v} \rangle) / \rho_0])_\phi$  in stead of  $[\nabla \times (\langle \mathbf{v} \times \boldsymbol{\omega} \rangle)]_\phi$ . Then we define the momentum flux on the meridional plane as:

$$\langle F_{ij} \rangle = \tilde{F}_{ij} + F'_{ij} \tag{C5}$$

$$\tilde{F}_{ij} = \rho_0 \langle v_i \rangle \langle v_j \rangle, \tag{C6}$$

$$F'_{ij} = \rho_0 \langle v'_i v'_j \rangle, \tag{C7}$$

where  $i$  and  $j$  correspond to  $r$ ,  $\theta$ , and  $\phi$ . For this definition, we divide the velocity as  $v_i = \langle v_i \rangle + v'_i$ . Then the divergence of the fluxes are divided to several terms as:

$$\mathbf{D} = -\frac{1}{\rho_0} \nabla \cdot \mathbf{F} = D_r \mathbf{e}_r + D_\theta \mathbf{e}_\theta, \quad (\text{C8})$$

$$D_r = D_{r(\text{d})} + D_{r(\text{n})}, \quad (\text{C9})$$

$$D_\theta = D_{\theta(\text{d})} + D_{\theta(\text{n})}, \quad (\text{C10})$$

$$D_{r(\text{d})} = -\frac{1}{\rho_0} \left[ \frac{1}{r^2} \frac{\partial}{\partial r} (r^2 F_{rr}) - \frac{F_{\theta\theta}}{r} \right], \quad (\text{C11})$$

$$D_{r(\text{n})} = -\frac{1}{\rho_0 r \sin \theta} \frac{\partial}{\partial \theta} (\sin \theta F_{\theta r}), \quad (\text{C12})$$

$$D_{\theta(\text{d})} = -\frac{1}{\rho_0} \frac{1}{r \sin \theta} \frac{\partial}{\partial \theta} (\sin \theta F_{\theta\theta}), \quad (\text{C13})$$

$$D_{\theta(\text{n})} = -\frac{1}{\rho_0} \left[ \frac{1}{r^2} \frac{\partial}{\partial r} (r^2 F_{r\theta}) + \frac{F_{\theta r}}{r} \right], \quad (\text{C14})$$

$$D_{r\phi} = \frac{F_{\phi\phi}}{r \rho_0}, \quad (\text{C15})$$

$$D_{\theta\phi} = \cot \theta \frac{F_{\phi\phi}}{r \rho_0}, \quad (\text{C16})$$

We use the notation of  $\tilde{D} = D(\tilde{F})$  and  $D' = D(F')$ . Then the zonal component of the curl of the  $\langle \mathbf{D} \rangle$  is also divided to several terms as:

$$\mathcal{C} = (\nabla \times \langle \mathbf{D} \rangle)_\phi = \mathcal{C}_r + \mathcal{C}_\theta + \mathcal{C}_\text{d}. \quad (\text{C17})$$

Then each term is divided  $\mathcal{C}_i = \tilde{\mathcal{C}}_i + \mathcal{C}'_i$ , where  $i$  corresponds to  $r, \theta, d$ . The terms are

$$\tilde{\mathcal{C}}_r = -\frac{1}{r} \frac{\partial \tilde{D}_{r(n)}}{\partial \theta}, \quad \mathcal{C}'_r = -\frac{1}{r} \frac{\partial D'_{r(n)}}{\partial \theta}, \quad (\text{C18})$$

$$\tilde{\mathcal{C}}_\theta = \frac{1}{r} \frac{\partial}{\partial r} (r \tilde{D}_{\theta(n)}), \quad \mathcal{C}'_\theta = \frac{1}{r} \frac{\partial}{\partial r} (r D'_{\theta(n)}), \quad (\text{C19})$$

$$\tilde{\mathcal{C}}_d = \frac{1}{r} \frac{\partial}{\partial r} (r \tilde{D}_{\theta(d)}) - \frac{1}{r} \frac{\partial \tilde{D}_{r(d)}}{\partial \theta}, \quad (\text{C20})$$

$$\mathcal{C}'_d = \frac{1}{r} \frac{\partial}{\partial r} [r(D'_{\theta(d)} + D'_{\theta\phi})] - \frac{1}{r} \frac{\partial}{\partial \theta} (D'_{r(d)} + D'_{r\phi}), \quad (\text{C21})$$

$$\begin{aligned} \mathcal{T}_1 &= \frac{1}{r} \frac{\partial}{\partial r} (r \tilde{D}_{\theta\phi}) - \frac{1}{r} \frac{\partial \tilde{D}_{r\phi}}{\partial \theta}, \\ &= \frac{\sin \theta \cos \theta}{r} \frac{\partial}{\partial r} (r^2 \langle \Omega_1 \rangle^2) - \frac{\partial}{\partial \theta} (\sin^2 \theta \langle \Omega_1 \rangle^2) \\ &= r \sin \theta \frac{\partial \langle \Omega_1 \rangle^2}{\partial z}. \end{aligned} \quad (\text{C22})$$

We note that the contribution of the mean differential rotation  $\langle \Omega_1 \rangle$  is separated with using the term  $\mathcal{T}_1$ . Then the eq. (C1) is averaged in time and zonal direction. The equation of the balance is obtained as:

$$\mathcal{W} - \mathcal{T} = \mathcal{B} + \mathcal{C} + \mathcal{V}, \quad (\text{C23})$$

$$(\text{C24})$$

where

$$\mathcal{W} = \frac{\partial \langle \omega_\phi \rangle}{\partial t}, \quad (\text{C25})$$

$$\begin{aligned} \mathcal{T} &= \mathcal{T}_0 + \mathcal{T}_1, \\ &= r \sin \theta \frac{\partial \langle \Omega \rangle^2}{\partial z}, \end{aligned} \quad (\text{C26})$$

$$\mathcal{B} = - \left[ \nabla \times \left( \frac{\nabla p_1 + \rho_1 g \mathbf{e}_r}{\rho} \right) \right]_\phi, \quad (\text{C27})$$

$$\mathcal{V} = [\langle \nabla \times \mathbf{G} \rangle]_\phi. \quad (\text{C28})$$

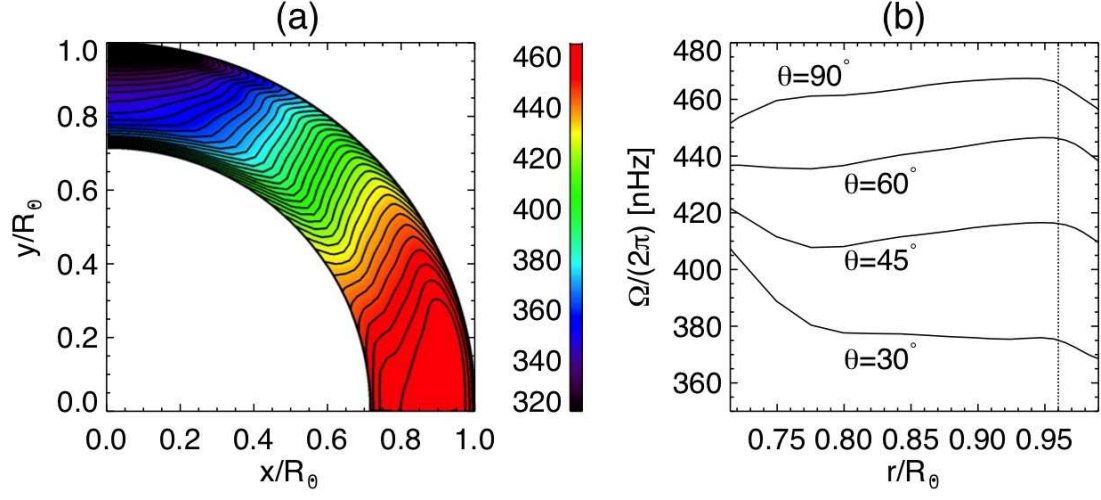


Fig. 1.— An inversion of the helioseismology from HMI data about the angular velocity ( $\Omega/2\pi$ ) in the unit of nHz (Howe et al. 2011) (a) on meridional plane and (b) along the selected colatitude. The dashed line in the panel b roughly shows the bottom of the NSSL.



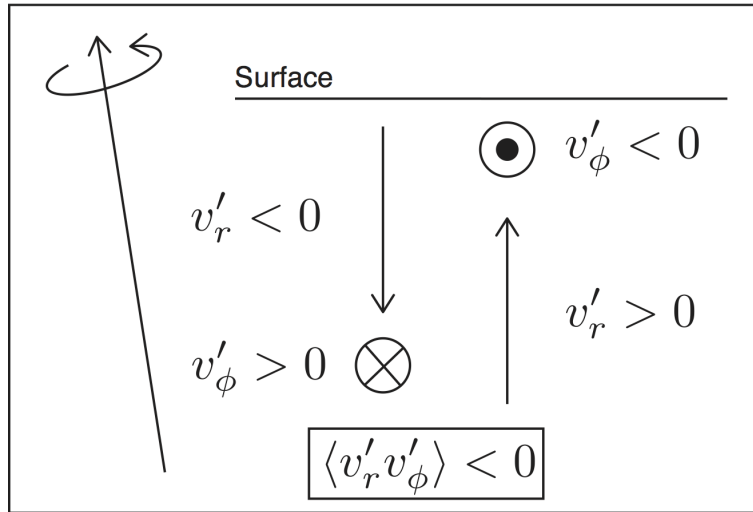


Fig. 2.— Schematic of the inward angular momentum transport by the radial velocity under the weak influence from the rotation.

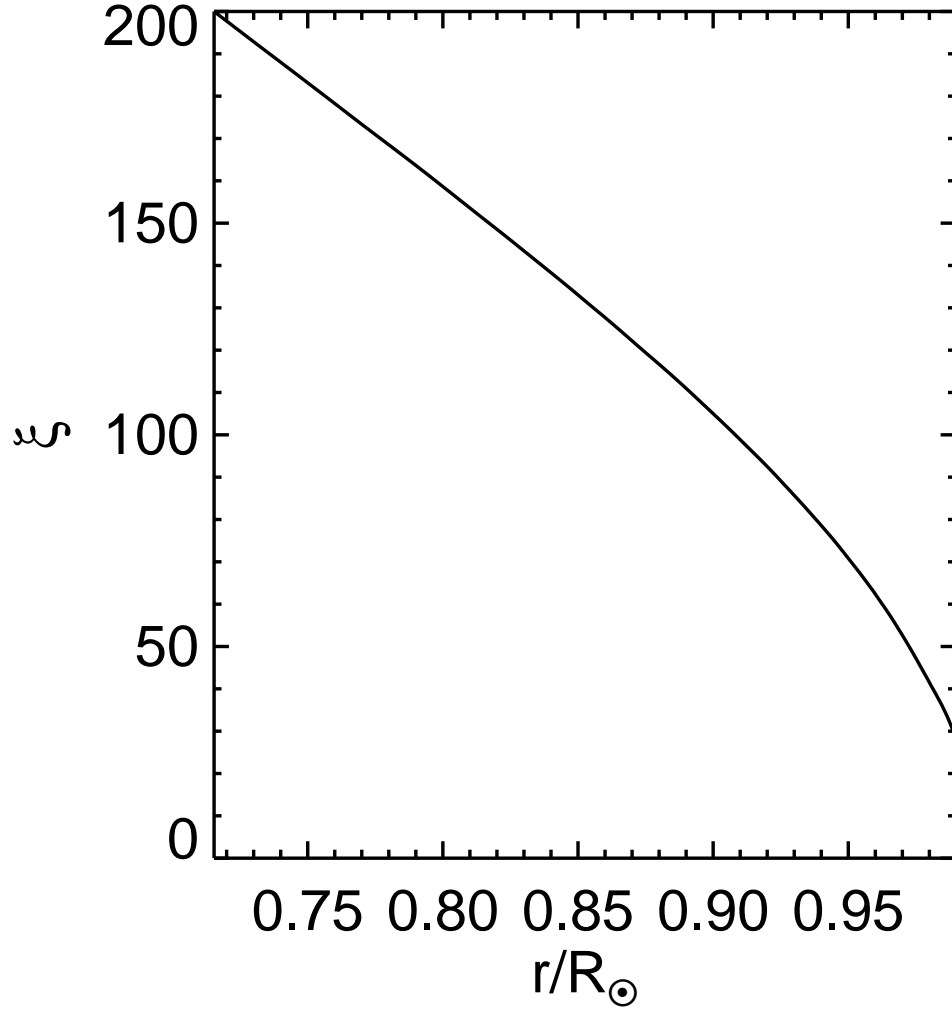


Fig. 3.— The distribution of  $\xi$ .

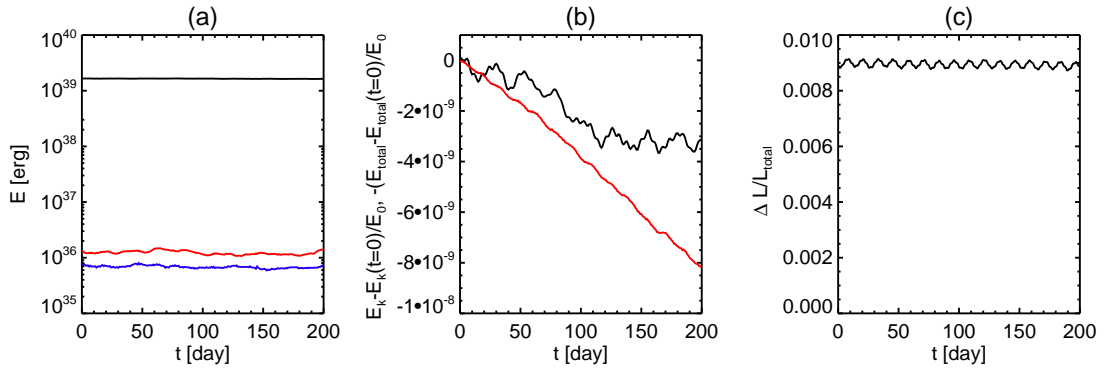


Fig. 4.— (a) Temporal evolution of total kinetic energy of mean velocity. The blue, red, black lines show the total kinetic energy of  $\langle v_r \rangle$ ,  $\langle v_\theta \rangle$ , and  $\langle v_\phi \rangle$ , respectively. (b) Temporal evolution of the difference of total kinetic energy including differential rotation, meridional flow and non-axisymmetric flow (black) and total energy including internal energy  $\rho e_1 + \rho v^2/2$  (red) from the value at  $t = 0$  normalized by the background internal energy, i.e., the initial total energy. (c) Temporal evolution of the deviation of the angular momentum conservation using the ratio to the total angular momentum.

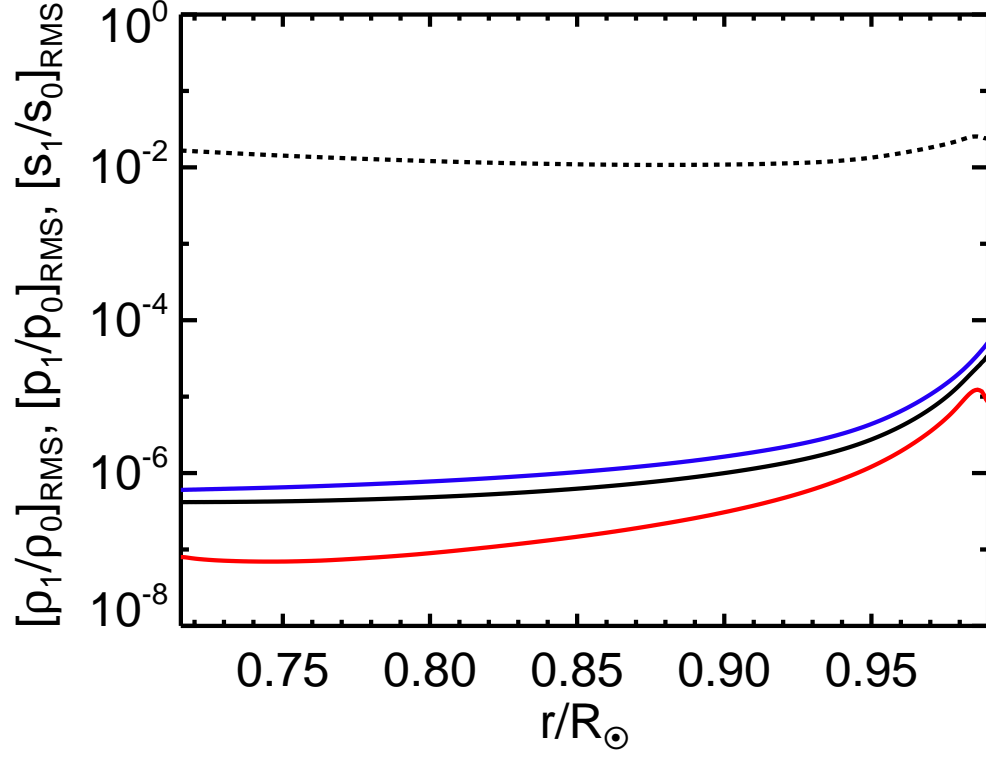


Fig. 5.— The radial distribution of RMS values of  $\rho_1/\rho_0$  (black),  $p_1/p_0$  (blue) and  $s_1/c_p$  (red). The dashed line shows RMS value of  $\xi^2 \rho_1/\rho_0$

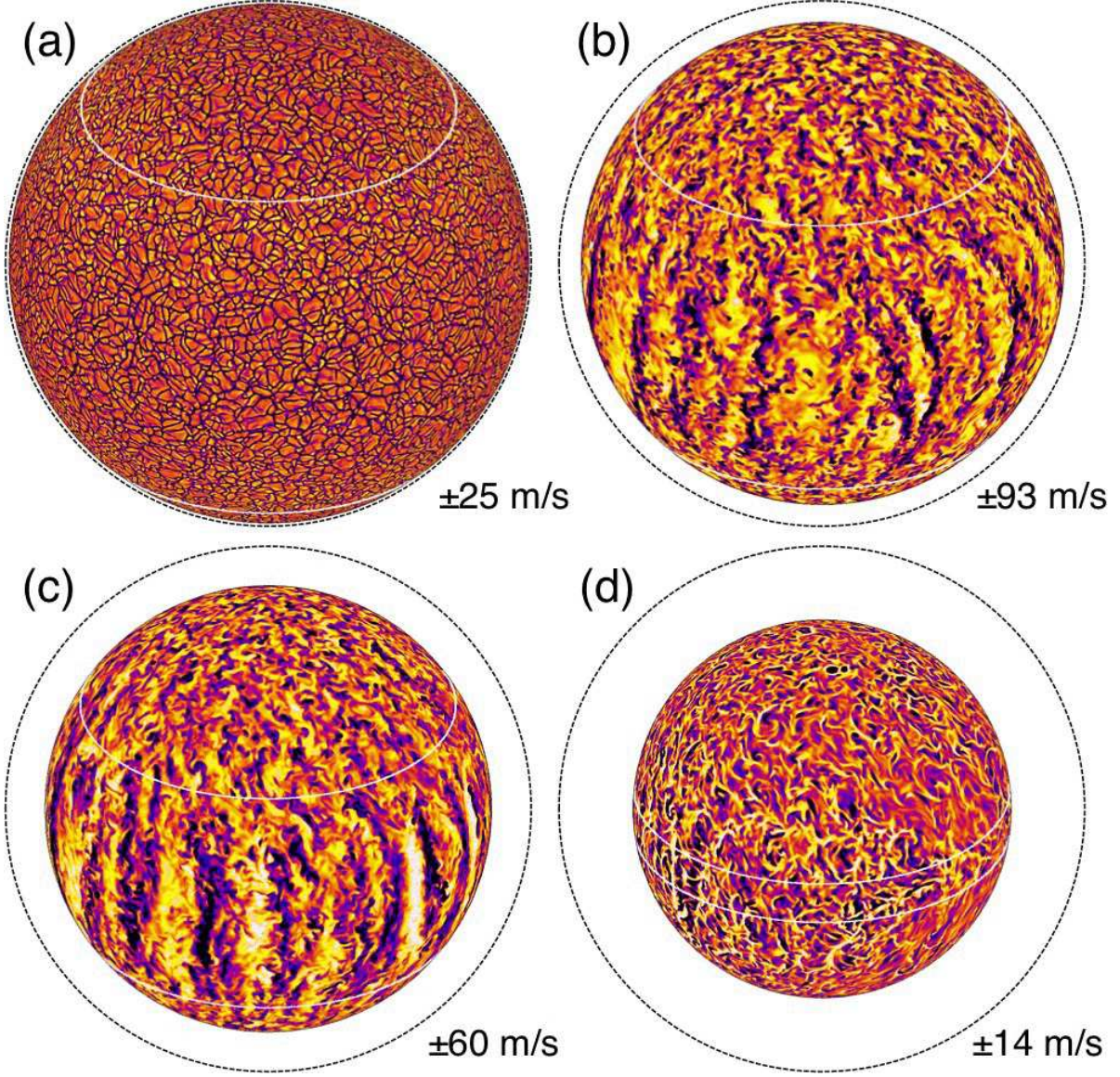


Fig. 6.— Contour of the radial velocity  $v_r$  at (a)  $r = 0.99R_\odot$  (b)  $r = 0.92R_\odot$ , (c)  $r = 0.85R_\odot$ , (d)  $r = 0.72R_\odot$ . The white lines show the tangential cylinder  $r \sin \theta = r_{\min}$ , where  $r_{\min} = 0.715R_\odot$ .

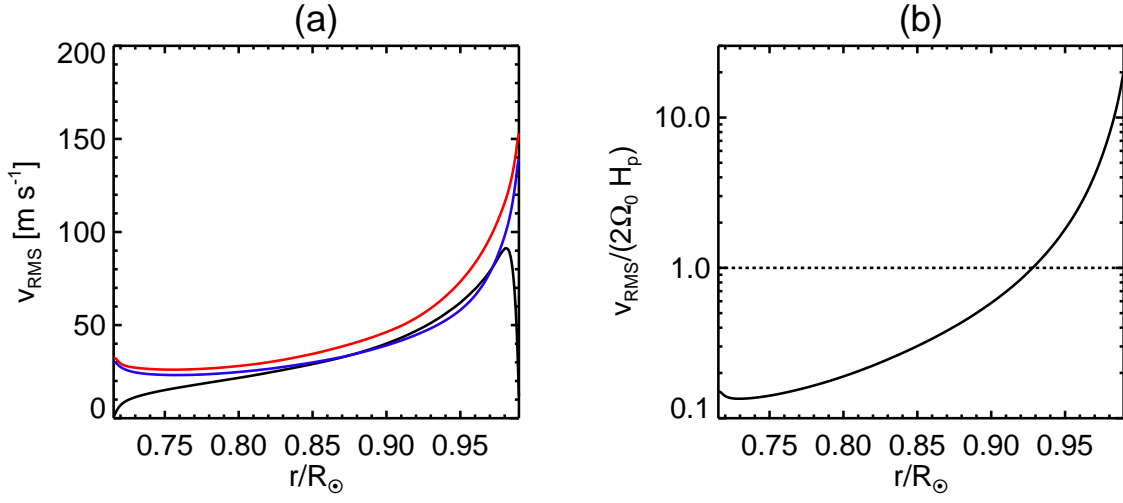


Fig. 7.— The radial profile of (a) the RMS velocity and (b)  $v_{\text{RMS}}/(2\Omega_0 H_p)$ . The black, blue and red lines show the radial ( $v_r$ ), the latitudinal ( $v_\theta$ ), and the zonal ( $v_\phi$ ) values, respectively. The dashed line in the panel b indicates the values at unity.

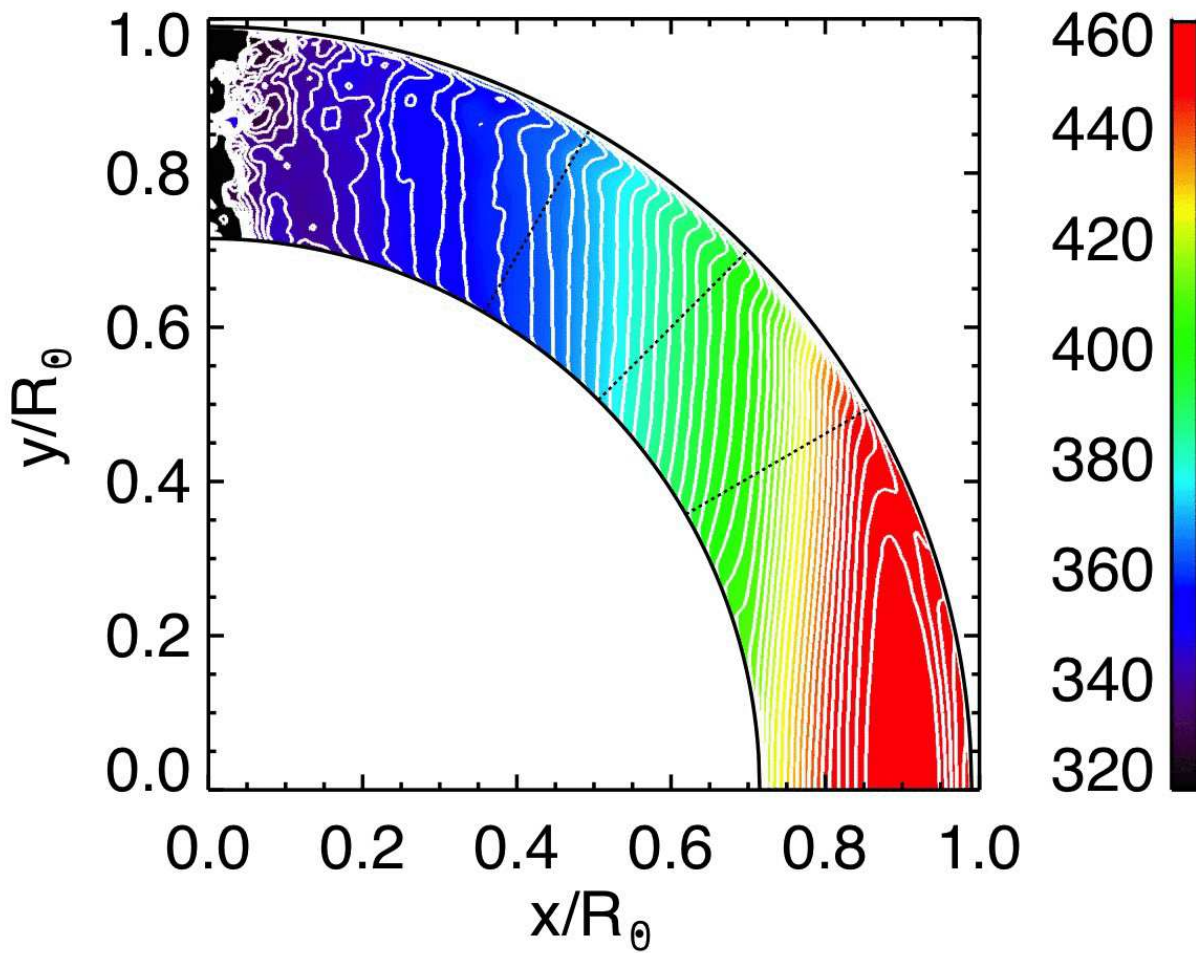


Fig. 8.— The averaged angular velocity ( $\langle \Omega \rangle / (2\pi)$ ) over 200 days in the unit of nHz. The black dashed lines show the selected colatitude in Fig. 9.

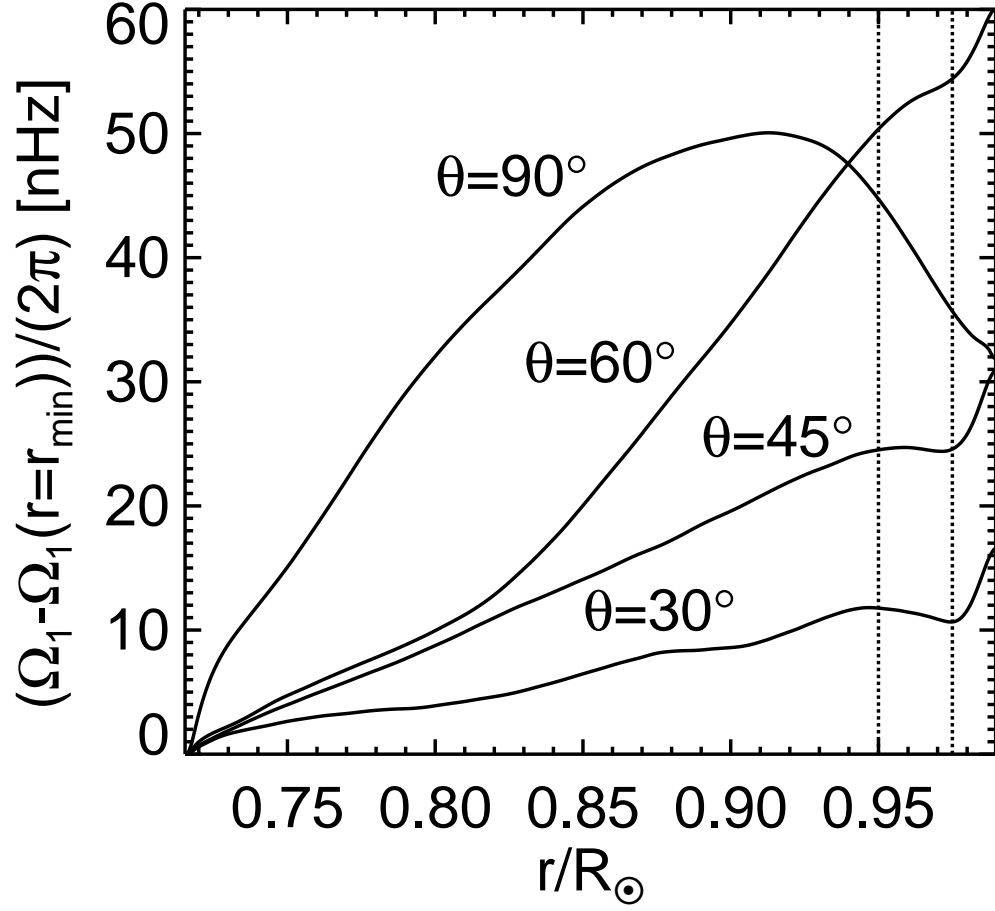


Fig. 9.— The radial profile of the angular velocity on the selected colatitudes. The dotted lines shows  $r = 0.95R_{\odot}$  and  $0.975R_{\odot}$ , which is roughly the NSSL.



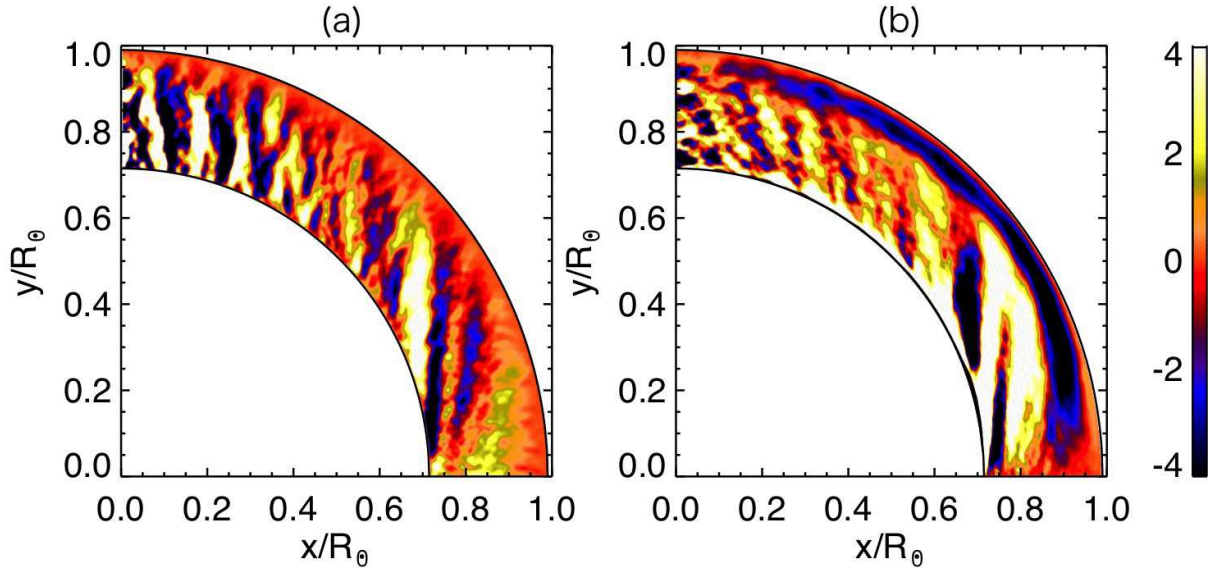


Fig. 10.— The radial and latitudinal mass fluxes averaged in time and zonal direction over 200 days. (a)  $\rho_0 \langle v_r \rangle$  and (b)  $\rho_0 \langle v_\theta \rangle$  in the unit of  $\text{g cm}^{-2} \text{s}^{-1}$ .

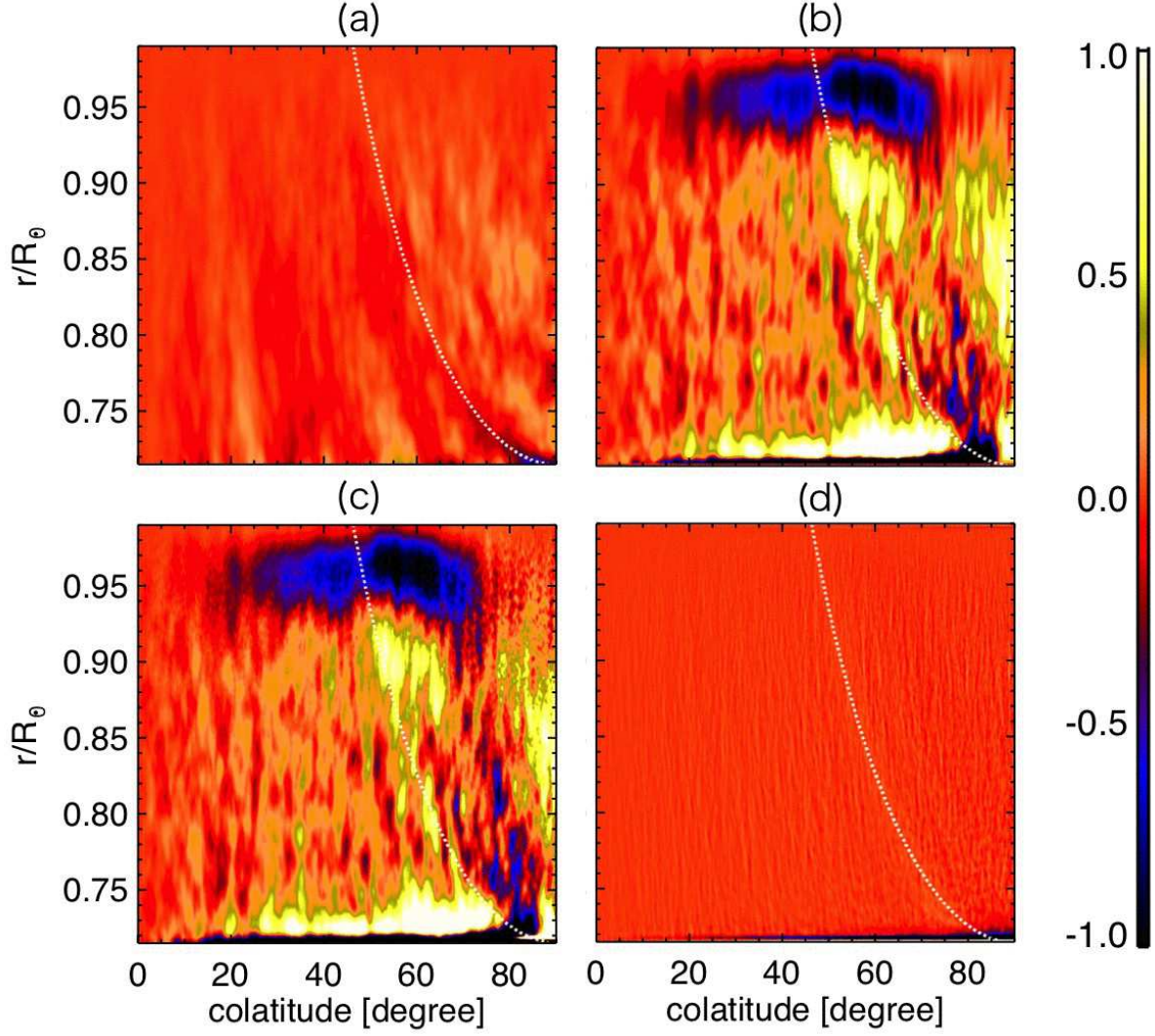


Fig. 11.— The values (a)  $\rho_0 \partial \langle \mathcal{L} \rangle / \partial t$ , (b)  $\rho_0 \langle \mathbf{v}_m \rangle \cdot \langle \mathcal{L} \rangle$ , (c)  $-\rho_0 \langle (\mathbf{v}'_m \cdot \nabla) \mathcal{L}' \rangle$  and (d)  $-\rho_0 r \sin \theta \langle \nabla \cdot \mathbf{F}_{v_\phi} / \rho \rangle$  in the unit of  $10^6 \text{ g cm}^{-1} \text{ s}^{-2}$  are shown on the meridional plane. The white lines show the location of the tangential cylinder.

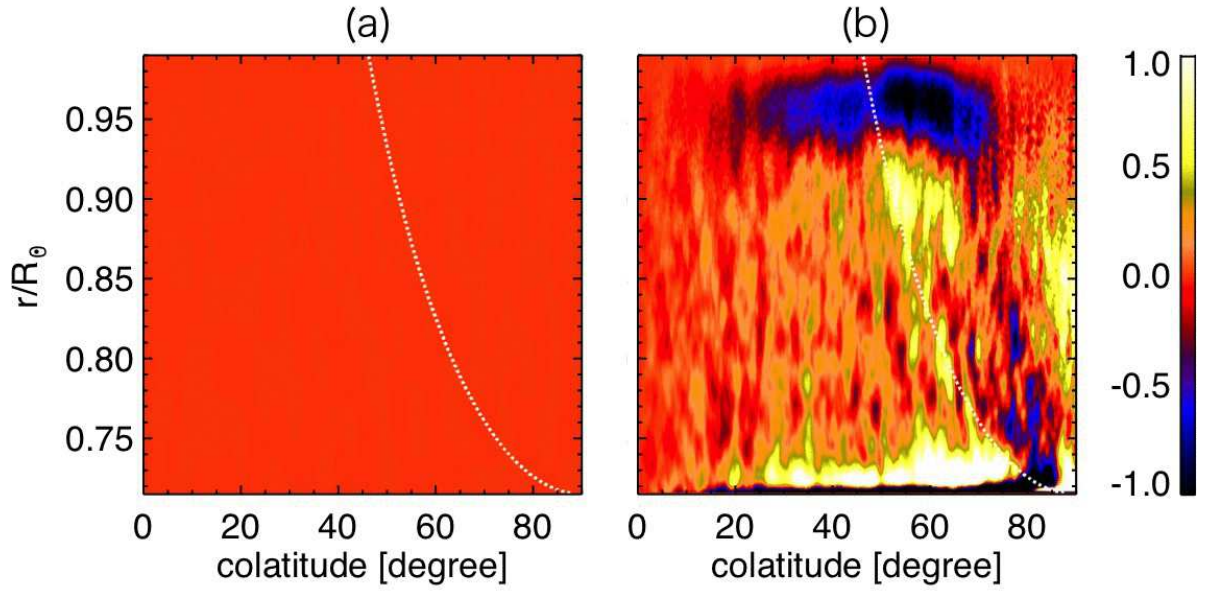


Fig. 12.— The values (a)  $\langle \mathcal{L} \nabla \cdot (\rho \mathbf{v}) \rangle$  and (b)  $-\nabla \cdot (\rho_0 \langle \mathbf{v}'_{\text{m}} \mathcal{L}' \rangle)$ , in the unit of  $10^6 \text{ g cm}^{-1} \text{ s}^{-2}$  are shown on the meridional plane. The white lines show the location of the tangential cylinder.

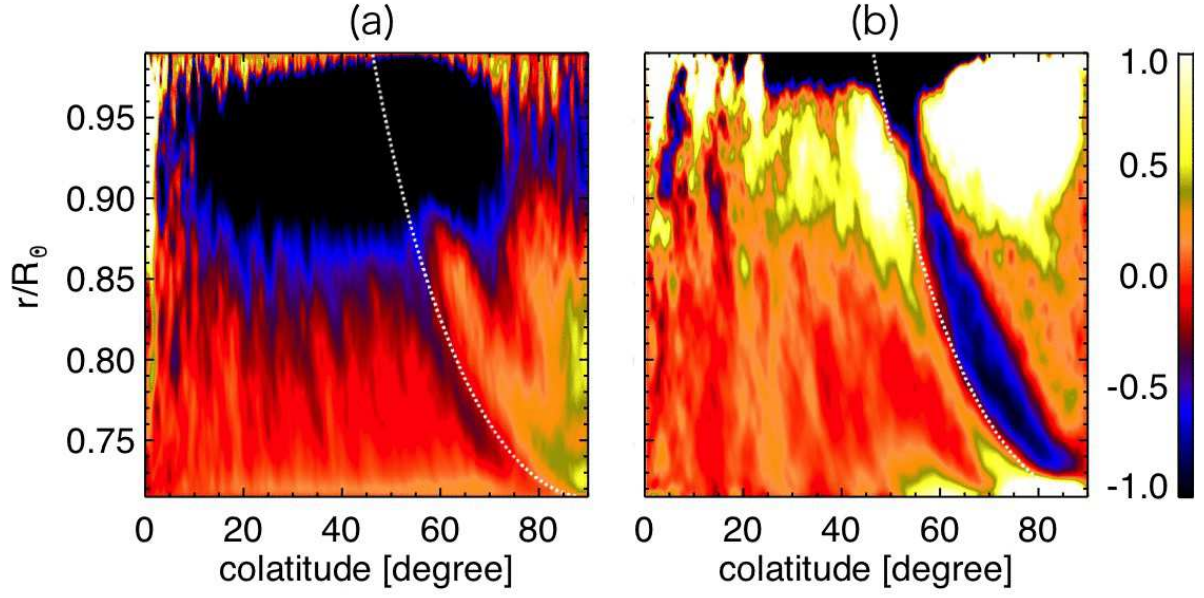


Fig. 13.— The values (a)  $\langle v'_r v'_\phi \rangle$ , and (b)  $\langle v'_\theta v'_\phi \rangle$  in the unit of  $10^6 \text{ cm}^2 \text{ s}^{-2}$  in the unit of  $10^6 \text{ g cm}^{-1} \text{ s}^{-2}$  are shown on the meridional plane. The white lines show the location of the tangential cylinder.

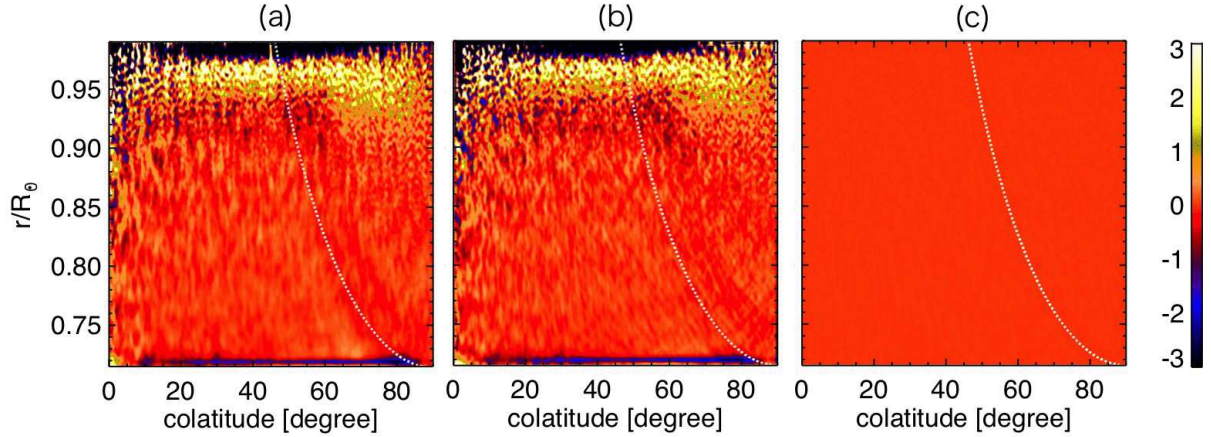


Fig. 14.— The values (a)  $\nabla \times (\langle \mathbf{v} \times \omega \rangle)$ , (b)  $\mathcal{C} = -\nabla \times [\nabla \cdot (\rho_0 \langle \mathbf{v} \mathbf{v} \rangle)] / \rho_0$ , and (c)  $\nabla \times [\langle \mathbf{v} \nabla \cdot (\rho \mathbf{v}) / \rho \rangle]$  are shown in the unit of  $10^{-12} \text{ s}^{-2}$  are shown on the meridional plane. The white lines show the location of the tangential cylinder.



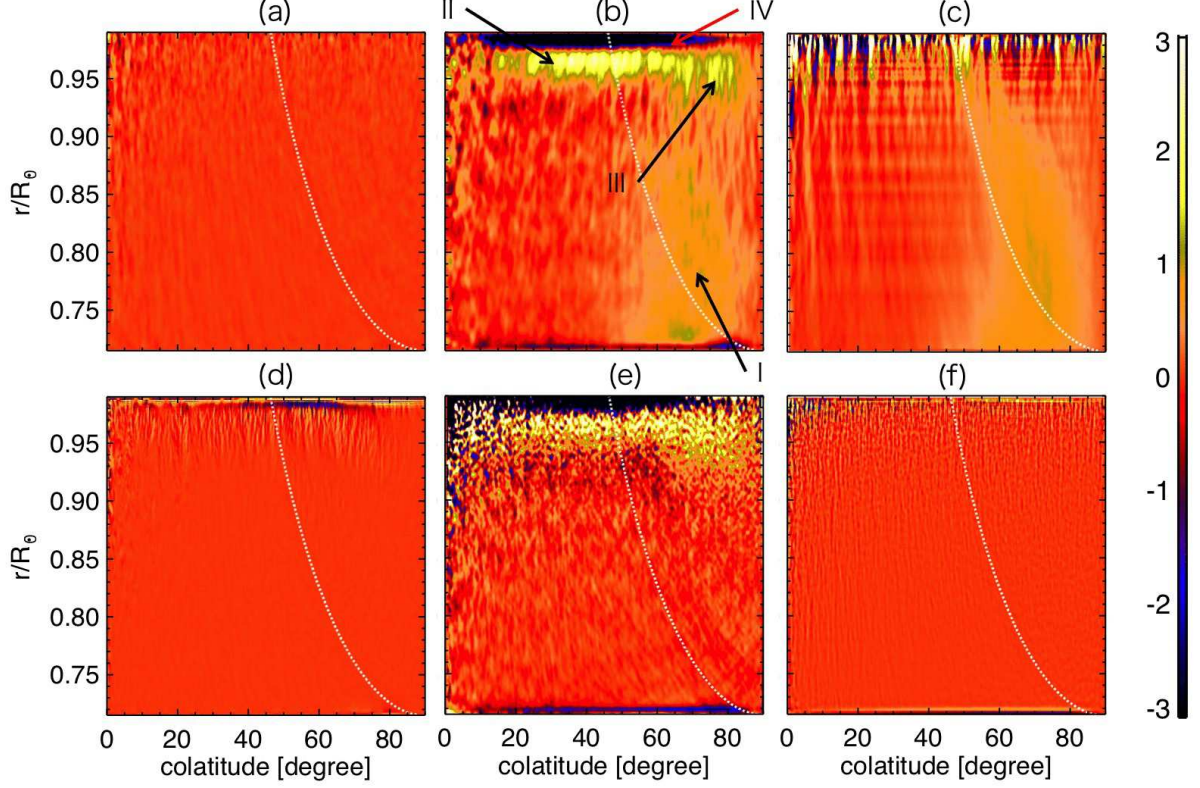


Fig. 15.— The values (a)  $\mathcal{W}$ , (b)  $-\mathcal{T}$ , (c)  $\mathcal{B}$ , (d)  $\tilde{\mathcal{C}}$ , (e)  $\mathcal{C}'$ , and (f)  $\mathcal{V}$  are shown in the unit of  $10^{-12} \text{ s}^{-2}$  are shown on the meridional plane. The white lines show the location of the tangential cylinder. The indicated regions I-IV refer to different balances achieved: I:  $-\mathcal{T} = \mathcal{B}$ , II, III, and IV:  $-\mathcal{T} = \mathcal{C}'$ .

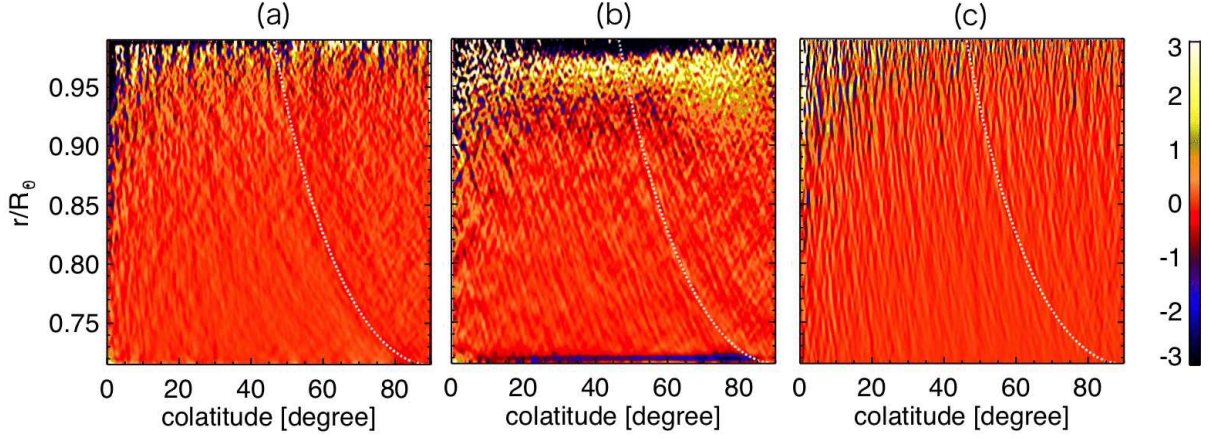


Fig. 16.— The values (a)  $C'_d$  (b)  $C'_\theta$ , and (c)  $C'_r$  in the unit of  $10^{-12} \text{ s}^{-2}$ , are shown on the meridional plane. The white lines show the location of the tangential cylinder.

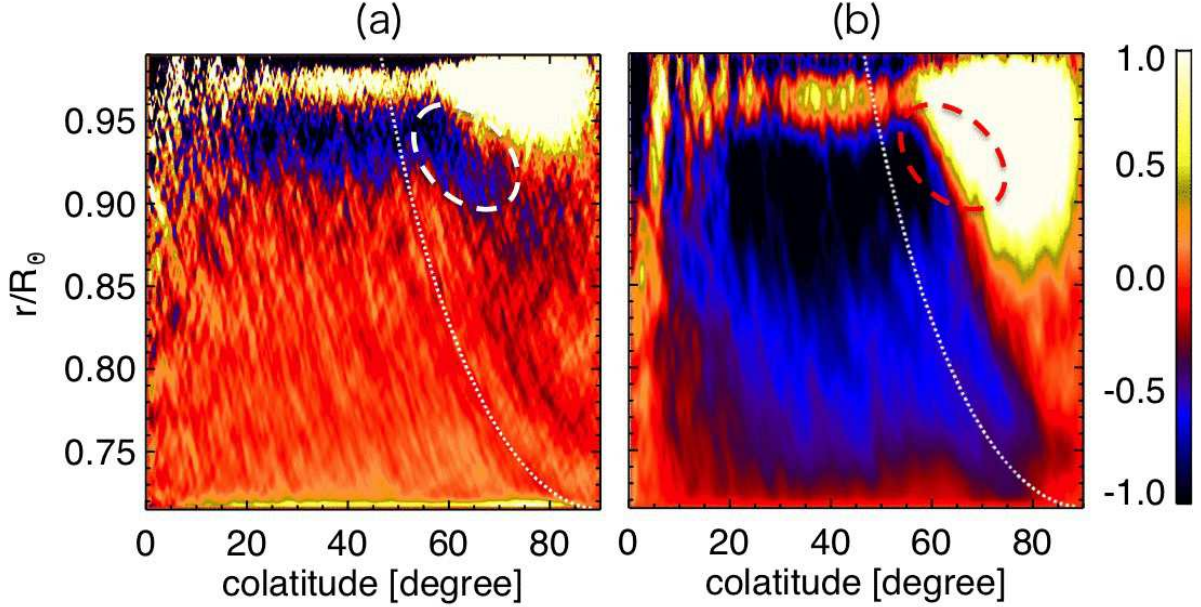


Fig. 17.— The values (a)  $D_{\theta(n)}$  in the unit of  $10^{-3} \text{ cm s}^{-2}$  and (b)  $\langle v'_r v'_\theta \rangle$  in the unit of  $10^6 \text{ cm}^2 \text{ s}^{-2}$  are shown on the meridional plane. The white lines show the location of the tangential cylinder. Dashed circle shows the boundary of the effective and ineffective area of the banana cell.

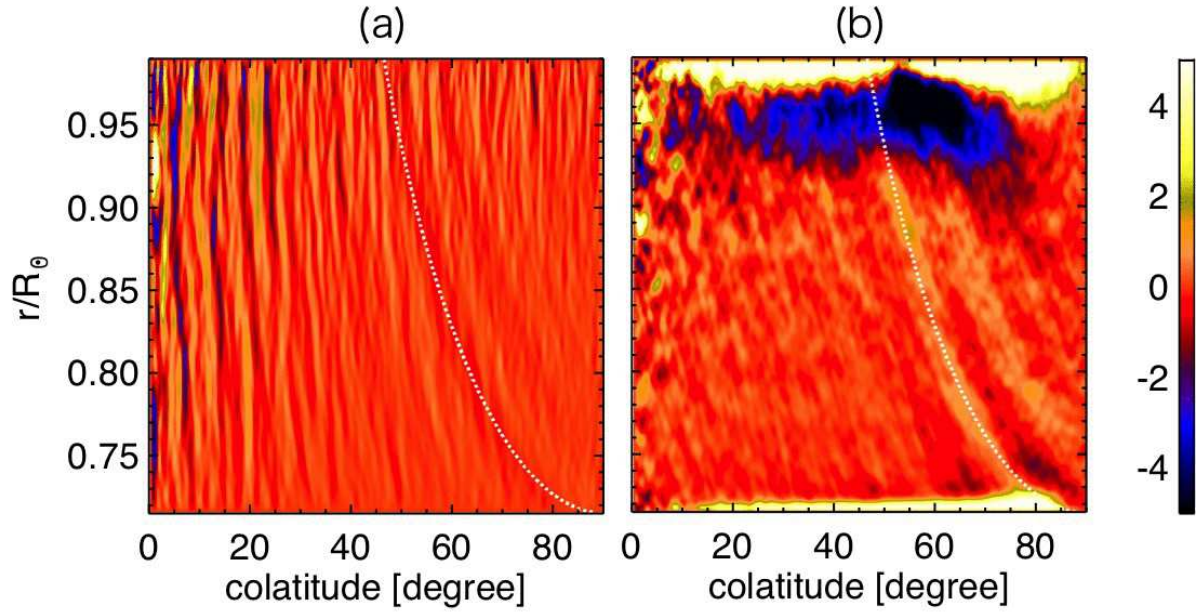


Fig. 18.— The values (a)  $\partial\langle v_r \rangle / (r\partial\theta)$ , and (b)  $\partial\langle v_\theta \rangle / \partial r$  in the unit of  $10^{-7} \text{ s}^{-1}$  are shown on the meridional plane. The white lines show the location of the tangential cylinder.

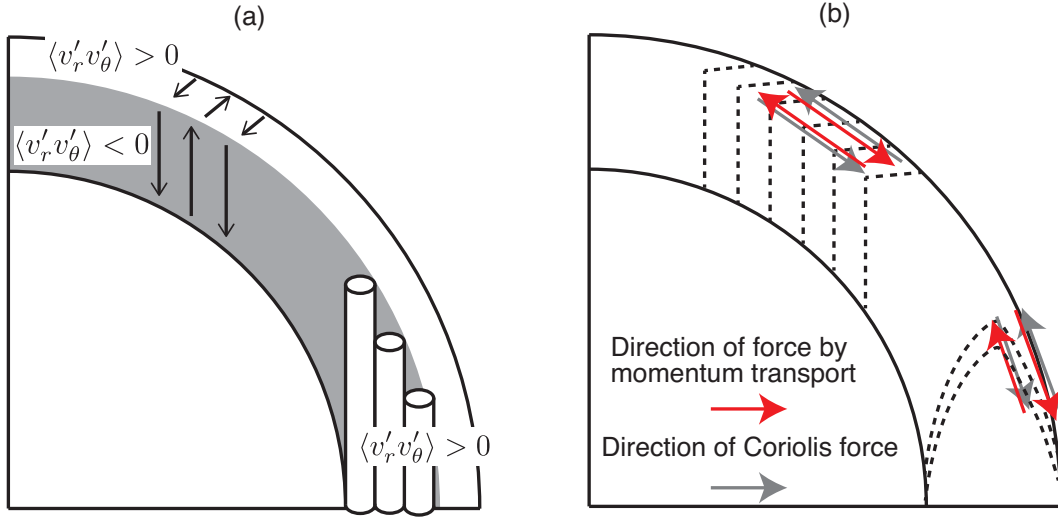


Fig. 19.— The summary of our findings in the schematic picture. In this figure we only discuss Reynolds-stress related balances, i.e. we do not show the thermal wind balance in the bulk of the convection zone. The panel a shows the distribution of the correlation  $\langle v'_r v'_\theta \rangle$ . The gray area indicates the strong influence of the rotation. The panel b shows the force balance on the meridional plane. The gray and red arrows show the direction of the Coriolis force and the force by the momentum transport. Regarding the Coriolis force, the latitudinal component is shown. The dashed lines are the contour line of the angular velocity.



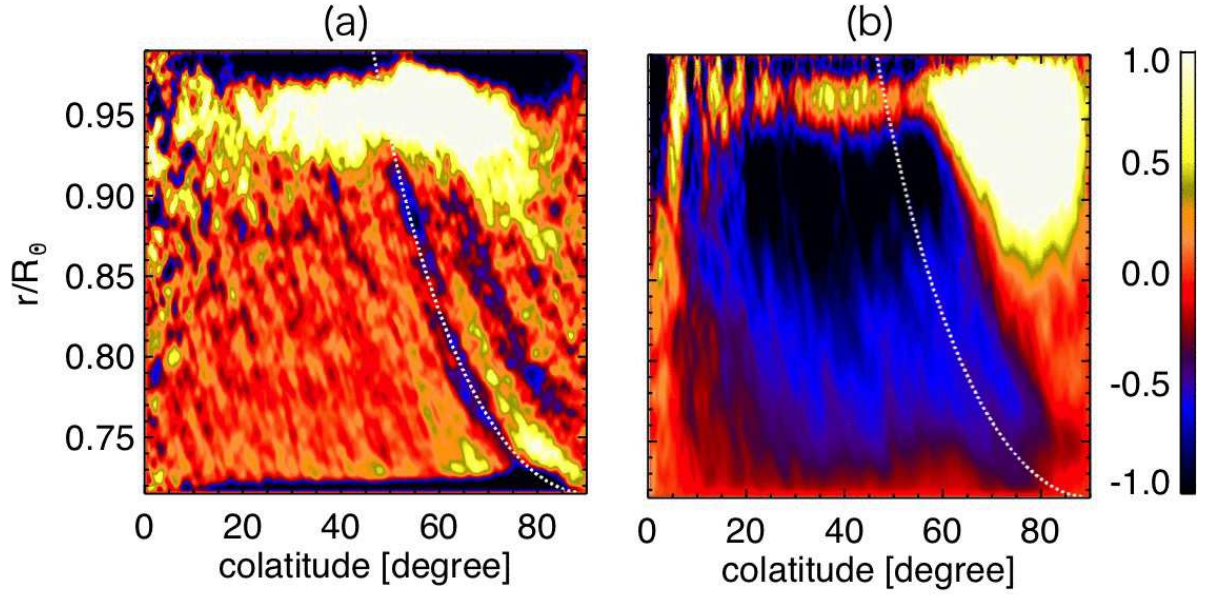


Fig. 20.— (a) The quantity  $-v_{\text{RMS}} H_p r \partial(\langle v_\theta \rangle / r) / \partial r / 3$  is shown, which indicates stress by the turbulent viscosity and (b)  $\langle v'_r v'_\theta \rangle$  for a easy comparison in the unit of in the unit of  $10^6 \text{ cm}^2 \text{ s}^{-2}$ .